The Spc105/Kre28 complex promotes mitotic error correction by outer kinetochore recruitment of Ipl1/Sli15

Alexander Dudziak[1], Richard Pleuger[1], Jasmin Schmidt[1], Frederik Hamm[1], Sharvari Tendulkar[1], Karolin Jänen[1], Ingrid R. Vetter[2], Sylvia Singh[3], Josef Fischböck[3], Franz Herzog[3,4] and Stefan Westermann[1]

[1]Department of Molecular Genetics I, Faculty of Biology, Center of Medical Biotechnology, University of Duisburg-Essen, Universitätsstrasse 5, 45117 Essen, Germany

[2]Department of Mechanistic Cell Biology, Max-Planck-Institute of Molecular Physiology, Otto-Hahn-Straße 11, 44227 Dortmund, Germany

[3]Gene Center Munich and Department of Biochemistry, Ludwig-Maximilians-Universität München, Feodor-Lynen-Str. 25, 81377 Munich, Germany

[4]Institute Krems Bioanalytics, IMC University of Applied Sciences, Krems, Piaristengasse 1, A-3500 Krems, Austria

[#]correspondence to: Stefan.Westermann@uni-due.de

Abstract

Kinetochores link chromosomes to dynamic microtubules of the mitotic spindle. To ensure equal chromosome segregation, sister chromatids must achieve biorientation. The conserved kinase Aurora B phosphorylates outer kinetochore proteins on attachments lacking tension, allowing re-establishment of new connections until biorientation is achieved. Aurora B localizes to the centromere as part of the chromosomal passenger complex (CPC), but the underlying recruitment pathways can be eliminated without disrupting biorientation. It therefore remains unclear how the kinase operates during error correction. Here, we identify the conserved Spc105/Kre28 complex as an outer kinetochore receptor of the Aurora kinase Ipl1 and its activator Sli15 in *Saccharomyces cerevisiae*. We show that mutations in the helix bundle domain of Spc105/Kre28 impair mitotic error correction, resembling the effects of *ipl1* or *sli15* mutants. The defects can be suppressed by artificial recruitment of Ipl1. In biochemical experiments Ipl1/Sli15 directly associates with Spc105/Kre28, and a conserved segment in the Sli15 central domain is crucially involved in the binding mechanism. These results have important implications for the mechanism of tension-dependent error correction during chromosome biorientation.

Keywords: chromosome biorientation; error correction; chromosomal passenger complex; KMN network; signaling

Introduction

Faithful chromosome segregation during mitosis depends on the physical interaction between highly dynamic microtubules of the mitotic spindle and kinetochores which assemble on centromeric DNA of each sister chromatid. Kinetochores are megadalton-sized proteinaceous structures consisting of multiple subcomplexes which fulfill different functions and assemble in a hierarchical manner. The constitutive centromere-associated network (CCAN) is the main constituent of the inner kinetochore (Dendooven *et al*, 2023; Pesenti *et al*, 2022; Yatskevich *et al*, 2022) which is recruited to centromeres through the interaction of the Mif2^{CENP-C} subunit with centromeric nucleosomes (Kato *et al*, 2013; Xiao *et al*, 2017). The CCAN consecutively recruits subcomplexes of the outer kinetochore generally termed as KMN network which consists of the Spc105^{Knl1}/Kre28^{Zwint} complex, Mtw1 complex (Mtw1, Dsn1, Nnf1, Nsl1) and Ndc80 complex (Ndc80, Nuf2, Spc24, Spc25) (Polley *et al*, 2024; Yatskevich *et al*, 2024). In this context, the Mtw1 complex serves as scaffold which connects the other KMN subcomplexes with the inner kinetochore by direct association with Mif2^{CENP-C} and Ame1^{CENP-U} (Dimitrova *et al*, 2016; Hornung *et al*, 2014; Musacchio & Desai, 2017; Petrovic *et al*, 2016; Weir *et al*, 2016). The highly elongated Ndc80 complex is the main microtubule receptor of the kinetochore which binds to the mitotic spindle through the calponin homology (CH) domains at the N-termini of the Ndc80 and Nuf2 subunits (Ciferri *et al*, 2008; Wei *et al*, 2007; Wilson-Kubalek *et al*, 2008). The Ndc80/Nuf2 head also recruits the checkpoint kinase Mps1 to the kinetochore (Parnell *et al*, 2024; Pleuger *et al*, 2024; Zahm & Harrison, 2024). The RWD domains of the Spc24 and Spc25 subunits connect the Ndc80 complex with the Mtw1 complex (Dimitrova *et al.*, 2016; Malvezzi *et al*, 2013; Petrovic *et al.*, 2016). Furthermore, the Mtw1 complex recruits Spc105^{Knl1}/Kre28^{Zwint} to the kinetochore, even though the molecular mechanisms differ between mammals and yeast (Ghodgaonkar-Steger *et al*, 2020; Petrovic *et al*, 2014; Roy *et al*, 2022). It has been well established that Spc105^{Knl1} plays a crucial role as a signaling platform for the spindle assembly checkpoint (SAC) after phosphorylation of MELT repeats by the conserved kinase Mps1 (London *et al*, 2012; Shepperd *et al*, 2012; Yamagishi *et al*, 2012). Furthermore, Spc105^{Knl1} is required for recruitment of different protein phosphatases which are involved in SAC silencing and modulation of kinetochore-microtubule attachments (Meadows *et al*, 2011; Nijenhuis *et al*, 2014; Rosenberg *et al*, 2011). In contrast, relatively little is known about Kre28^{Zwint} (also referred to as YDR532C according to its systematic name). Kre28 was identified as budding yeast homolog of the metazoan protein Zwint (Zeste White interacting protein) due its sequence similarity and, similar to Zwint, Kre28 forms a complex with Spc105^{Knl1} (Pagliuca *et al*, 2009). In contrast to mammalian cells, where the tandem RWD domains of Knl1 directly associate with the Mtw1 complex (Petrovic *et al.*, 2014), *S. cerevisiae* Kre28 itself binds to the Mtw1 complex and by this recruits Spc105^{Knl1} to the kinetochore (Ghodgaonkar-Steger *et al.*, 2020; Roy *et al.*, 2022). Both, the interaction with

Spc105^{Knl1} and with the Mtw1 complex is mediated by coiled-coil elements in the central region of Kre28 (Ghodgaonkar-Steger *et al.*, 2020; Roy *et al.*, 2022). Furthermore, the C-terminus of Kre28 (residues 299-386) forms an RWD domain whose function is unknown so far (Tromer *et al*, 2019). Kre28 is essential for viability of yeast cells (Pagliuca *et al.*, 2009). However, it is unclear whether this is just a consequence of loss of Spc105^{Knl1} from kinetochores or whether Kre28^{Zwint} has additional essential functions. For instance, it was proposed that Spc105^{Knl1}/Kre28^{Zwint} might be required for kinetochore localization of different microtubule-associated proteins (Pagliuca *et al.*, 2009).

The conserved protein kinase Ipl1$^{Aurora\ B}$ is an essential part of the error correction machinery which phosphorylates outer kinetochore substrates in order to release kinetochore-microtubule attachments that lack tension (Tanaka & Zhang, 2022). Ipl1$^{Aurora\ B}$ acts in a complex with Sli15^{INCENP}, Bir1^{Survivin} and Nbl1^{Borealin}, together termed as chromosomal passenger complex (CPC). The N-terminal CEN box of Sli15^{INCENP} associates with Bir1^{Survivin} and Nbl1^{Borealin} (Jeyaprakash *et al*, 2007) whereas its C-terminal IN box binds to the kinase domain of Ipl1$^{Aurora\ B}$ (Sessa *et al*, 2005). The CPC is targeted to the inner and kinetochore-proximal centromere by different mechanisms which depend on the haspin kinase, the Bub1 kinase and Sgo1/Sgo2 (Hindriksen *et al*, 2017). However, different studies have demonstrated that inner and kinetochore-proximal centromere localization of Ipl1$^{Aurora\ B}$ is dispensable for establishment of biorientation. For instance, an N-terminal deletion of Sli15, preventing inner centromere recruitment of the CPC through Bir1, still supports the formation of bioriented attachments (Campbell & Desai, 2013), suggesting that additional mechanisms can target the CPC to the kinetochore. Indeed, two recent studies identified the inner kinetochore COMA complex as a Bir1-independent Ipl1/Sli15 receptor (Fischbock-Halwachs *et al*, 2019; García-Rodríguez *et al*, 2019). Furthermore, studies in human cells have also suggested the existence of an additional pool of Aurora B at the kinetochore, which might be relevant for the phosphorylation of outer kinetochore proteins such as components of the KMN network (Broad *et al*, 2020; Hadders *et al*, 2020).

In this study, we provide a detailed molecular analysis of the KMN subunit Kre28^{Zwint}. We identified a conserved Zwint helix in Kre28 whose lack leads to fatal chromosome segregation defects when cells are forced to reform their spindle apparatus after nocodazole washout. Artificial recruitment of Ipl1 to the outer kinetochore is sufficient to suppress this phenotype. Using protein biochemistry, we demonstrate that Spc105^{Knl1}/Kre28^{Zwint} can directly recruit Ipl1$^{Aurora\ B}$/Sli15^{INCENP} *in vitro* and that a conserved segment of the Sli15 central domain is involved in the binding mechanism. Thus, we have identified Spc105/Kre28 as the elusive outer kinetochore receptor of Ipl1.

Results

Characterization of novel mutant alleles in the outer kinetochore subunit Kre28^{Zwint}

To gain insight into the organization of Spc105/Kre28 we performed AF2 structure predictions using the C-terminal part of Spc105 (omitting the disordered residues 1-489) and full-length Kre28 (**Figure 1A**). The model shows that the Spc105/Kre28 heterodimer is formed via two interfaces: At the C-terminus of Kre28 a single RWD domain (residues 299-385) is paired with the N-RWD domain of Spc105. Together with short alpha-helical segments just preceding these RWD domains, this part resembles heterodimeric RWD domain arrangements found in other kinetochore subunits like Spc24/Spc25 (Schmitzberger & Harrison, 2012). The N-terminal parts, on the other hand, engage into a helical bundle (**Figure 1A**). This is in agreement with previous studies that have established that Kre28 associates with Spc105 mainly via coiled-coil segments formed by residues 127-201 (Roy *et al.*, 2022), while another segment (229-259) is required for binding to the Mtw1 complex(Ghodgaonkar-Steger *et al.*, 2020). Deletion of these segments is incompatible with KMN assembly and yields lethal phenotypes in yeast. Interestingly, multiple sequence alignments show that an alpha-helical segment preceding the first Kre28 coiled-coil domain (residues 77-113, hereafter referred to as the Zwint helix) is among the most conserved segments of the protein (**Figure 1B**). By contrast, the C-terminus is not well conserved and human Zwint, for example, lacks an RWD domain (Tromer *et al.*, 2019).

To analyze the contribution of Zwint helix and RWD domain to Kre28 function in cells, we replaced the endogenous *KRE28* gene with Flag-tagged wildtype or mutant alleles in diploid cells (**Figure 1C**). Tetrad dissection showed that neither *kre28*$^{\Delta Zwint}$ nor *kre28*$^{\Delta RWD}$ alone impaired viability. However, haploid spores of the *kre28*$^{\Delta Zwint\ \Delta RWD}$ double mutant were never recovered, demonstrating that simultaneous elimination of these segments is lethal (**Figure 1C)**. Western blotting confirmed that wildtype and mutant proteins were expressed at comparable levels (**Figure 1D**). Interestingly, serial dilution assays of the haploid strains revealed that *kre28*$^{\Delta Zwint}$ mutants fully supported growth at 30 °C, but were inviable in the presence of the microtubule-depolymerizing drug benomyl and additionally displayed cold sensitivity **(Figure 1E**). By contrast the deletion of the C-terminal RWD domain of Kre28 did not cause a growth phenotype. We found that not only the complete removal of the Zwint helix, but also selected smaller deletions or point mutations of conserved residues caused benomyl hypersensitivity. The most pronounced phenotypes were obtained for truncations eliminating the c-terminal part of the helix spanning residues 103-113, as well as for point mutations in this region (**Figure EV1 A-D**).

156 **The *kre28$^{\Delta Zwint}$* mutant is defective in mitotic error correction of kinetochore-microtubule**
157 **attachments**

158 The pronounced benomyl hypersensitivity of the *kre28$^{\Delta Zwint}$* mutant may be caused by a defect
159 in the spindle assembly checkpoint (SAC) or a different problem with chromosome
160 segregation. To distinguish between these possibilities, we analyzed Pds1^{Securin} levels in
161 wildtype and *kre28$^{\Delta Zwint}$* strains after cells were released from a G1 arrest into medium
162 containing the microtubule-depolymerizing drug nocodazole. Both, wildtype and *kre28$^{\Delta Zwint}$*
163 mutant cells stabilized Pds1 levels, while a *mad1Δ* control strain failed to do so (**Figure 2A**).
164 Thus, *kre28$^{\Delta Zwint}$* cells have a functional SAC response to a lack of kinetochore-microtubule
165 attachments. To define the genetic relationship between the *kre28$^{\Delta Zwint}$* mutant and the mitotic
166 checkpoint more closely, we deleted the *MAD1* gene in the *KRE28* wildtype or *kre28$^{\Delta Zwint}$*
167 mutant background. Abolishing the SAC aggravated the growth defect of the *kre28$^{\Delta Zwint}$* mutant,
168 an effect that was particularly apparent at temperatures of 25 °C and 16 °C (**Figure 2B**). Thus,
169 the benomyl hypersensitivity of the *kre28$^{\Delta Zwint}$* mutant is not caused by a general mitotic
170 checkpoint defect, and indeed, the SAC is required to support viability of this mutant.
171 While *kre28$^{\Delta Zwint}$* mutant cells arrested efficiently in response to nocodazole, we found that
172 they nevertheless very quickly lost viability when cells were plated from nocodazole-containing
173 medium onto YEPD plates (**Appendix Figure S1**). To determine the reason for the rapid loss
174 in viability we arrested wildtype and mutant cells with nocodazole, then washed out the drug
175 to allow spindle reformation and chromosome attachment and followed the progression
176 through the first cell division. Analysis of Pds1 degradation kinetics showed that *kre28$^{\Delta Zwint}$*
177 mutant cells initiated anaphase – indicated by the decline in Pds1 levels - with the same timing
178 as wildtype cells **(Figure 2C**). The lack of a delay indicated that the SAC was not activated
179 under these conditions. In the same experimental setup, we analyzed the distribution of
180 fluorescently labelled chromosome XII (CEN12-GFP) following the nocodazole washout
181 (**Figure 2D**). Strikingly, *kre28$^{\Delta Zwint}$* mutant cells missegregated chromosome XII in nearly 70 %
182 of all anaphases, while wildtype cells displayed an error rate of less than 5% (**Figure 2E)**. This
183 high rate of missegregation can explain the pronounced benomyl hypersensitivity and the rapid
184 loss of viability after exposure to nocodazole.

185 The combination of phenotypes displayed by the *kre28$^{\Delta Zwint}$* mutant - a functional SAC in
186 response to microtubule depolymerization, but pronounced chromosome missegregation
187 without checkpoint activation following spindle reformation - is reminiscent of mutants in the
188 tension-dependent error correction pathway, such as *ipl1*, *sli15* or *sgo1* (Biggins & Murray,
189 2001; Indjeian *et al*, 2005). In genetic crosses we found that the *kre28$^{\Delta Zwint}$* mutant was highly
190 sensitive to further perturbations of the error correction machinery: Its combination with the

191 temperature-sensitive *ipl1-1* allele resulted in extremely poorly growing spores (**Figure 2F**) and
192 its combination with *sli15-3* or *sgo1Δ* was synthetic lethal. The genetic interactions of the
193 *kre28$^{\Delta Zwint}$* allele are summarized in **Figure 2G**. Deletion of the Kre28 Zwint helix is
194 synthetically lethal or aggravates growth defects when the function of the microtubule-binding
195 Ndc80 complex (*ndc80-1*) and Dam1 complex (*dam1-1*, *dam1-9* and *duo1$^{\Delta SxIP}$*) is
196 compromised. Furthermore, either direct perturbation of the CPC (*ipl1-1* and *sli15-3*) or
197 affecting its centromere (*sgo1Δ*) or inner kinetochore recruitment pathways (*ctf19$^{\Delta C\text{-}RWD}$*)
198 dramatically reduced cell growth in combination with the *kre28* mutant allele.
199

200 **The *kre28$^{\Delta Zwint}$* mutant reduces the level of Spc105/Kre28 at kinetochore clusters *in vivo***
201 To further define the molecular basis of the *kre28$^{\Delta Zwint}$* phenotype, we analyzed outer
202 kinetochore composition in wildtype and mutant cells by live cell imaging. The fluorescence
203 intensity of the KMN components Nuf2-GFP (Ndc80 complex) and Mtw1-GFP (Mtw1 complex)
204 at metaphase and anaphase kinetochore clusters was unaffected by the *kre28$^{\Delta Zwint}$* mutation
205 (**Figure 3A**). By contrast, we noticed a reduction of Spc105-GFP intensity at metaphase
206 kinetochores to about 70 % of the wildtype level and found that the apparent increase in cluster
207 intensity between metaphase and anaphase was reduced relative to the wildtype (**Figure 3B**).
208 These differences were not caused by changes in protein levels, as judged by western blotting
209 (**Figure EV2 A,B**). Since we found that a C-terminal GFP fusion caused a reduced protein
210 level of the *kre28$^{\Delta Zwint}$* mutant (**Figure EV2 C**), we constructed and analyzed N-terminal GFP-
211 fusions of wildtype and mutant alleles. GFP-Kre28$^{\Delta Zwint}$ was present at near wildtype levels in
212 western blots (**Figure EV2 B).** Similar to Spc105-GFP, the GFP-*kre28$^{\Delta Zwint}$* mutant displayed a
213 moderate reduction in metaphase kinetochore cluster intensity and a less pronounced increase
214 in apparent anaphase cluster intensity (**Figure 3B**). We conclude that the *kre28$^{\Delta Zwint}$* mutation
215 has a specific effect on the KMN network *in vivo*: It reduces the localization of Spc105/Kre28
216 to kinetochores without affecting the recruitment of Ndc80 and Mtw1 complexes.
217 Since Spc105 acts as a scaffold for the Mps1-dependent recruitment of Bub1/Bub3, we asked
218 if the Spc105 reduction would have any consequences on downstream signaling. We found
219 that Sgo1-GFP localization to kinetochores in prometaphase (which is dependent on Bub1)
220 was not affected by *kre28$^{\Delta Zwint}$*, suggesting that the modest reduction in Spc105 does not have
221 a pronounced effect on downstream signaling (**Figure EV2 E**). This is also consistent with the
222 observation that this mutant has a functional SAC.

223

224

225

226 **Artificial recruitment of Ipl1 to Mtw1 suppresses the *kre28$^{\Delta Zwint}$* phenotype *in vivo***

227 If the *kre28$^{\Delta Zwint}$* mutant reduces the association of Spc105/Kre28 to kinetochores *in vivo* and
228 the resulting phenotype resembles a lack of Ipl1 activity, then artificially increasing Ipl1
229 recruitment in the mutant may rescue the defect (**Figure 4A**). We tested this hypothesis by
230 constructing fusion proteins between the Mtw1 subunit (whose kinetochore level is unaffected
231 by *kre28$^{\Delta Zwint}$,* see **Figure 3**) and different C-terminal segments of the Sli15 protein. The fusions
232 were either prepared with wildtype Sli15 sequences or with two point mutations exchanging
233 conserved amino acids in the IN box (W646G, F680A), which prevent Ipl1 binding(Sessa *et*
234 *al.*, 2005). The genes encoding the fusion proteins were integrated as extra copies at the *lys2*
235 locus and expressed constitutively under control of the *MTW1* promoter (**Figure 4B, Appendix**
236 **Figure S2**).

237 Serial dilution assays showed that expression of neither fusion protein alone caused any
238 growth defects in a Kre28^{WT} strain background. Interestingly, Mtw1-Sli15$^{565-698}$ improved
239 growth of the *kre28$^{\Delta Zwint}$* mutant in the presence of benomyl. Moreover, the longer Mtw1-
240 Sli15$^{516-698}$ fusion, encompassing the IN box and the single alpha helix (SAH) domain, was
241 even more effective in suppressing the benomyl hypersensitivity of the *kre28$^{\Delta Zwint}$* mutant.
242 Importantly, fusion proteins with point mutations in the IN box had no beneficial effect on growth
243 of *kre28$^{\Delta Zwint}$* strains in the presence of benomyl, demonstrating the importance of Ipl1
244 recruitment to the outer kinetochore (**Figure 4C**).

245 We further analyzed the effect of the two Mtw1-Sli15 fusions on *kre28$^{\Delta Zwint}$* cells by scoring
246 segregation of fluorescently labelled chromosome XII in the first division after release from a
247 nocodazole arrest. As described before (see **Figure 2E**) about 70 % of *kre28$^{\Delta Zwint}$* cells
248 missegregated chromosome XII. In contrast, the rate of missegregation was significantly
249 reduced in *kre28$^{\Delta Zwint}$* cells expressing the Mtw1-Sli15 fusion proteins (**Figure 4D**). Similar to
250 the effect in the serial dilution assay, expression of the larger construct comprising Sli15
251 residues 516-698 showed a stronger suppression of the *kre28$^{\Delta Zwint}$* phenotype. Notably,
252 constitutive recruitment of Ipl1 the outer kinetochore via the Mtw1 fusion had no negative effect
253 on chromosome biorientation in a wildtype strain background.

254 These data indicate that insufficient Ipl1/Sli15 at the outer kinetochore is a main cause of the
255 phenotypes observed in *kre28$^{\Delta Zwint}$* strains.

256

257 **Ipl1/Sli15 directly binds the KMN network via the Spc105/Kre28 subcomplex**

258 We next asked whether the Ipl1/Sli15 complex may directly associate with the KMN network
259 and specifically with Spc105/Kre28. To this end we co-expressed the ten KMN subunits from
260 two separate baculoviruses in Sf9 insect cells and purified the network via a Flag tag at the C-
261 terminus of the Spc105 subunit. This purification strategy allowed the single-step isolation of a

262 stable full-length KMN network that co-eluted stoichiometrically during analytical size exclusion
263 chromatography (SEC) (**Figure 5A**). We evaluated the organization of the KMN network by
264 Pt/C rotary shadowing electron microscopy. In electron micrographs the Ndc80 complex (N)
265 was readily identifiable as a 50-60 nm long rod and its distal end was decorated by one or two
266 appendages – formed by the KM complexes - which seemed to adopt a variety of different
267 conformations relative to each other (**Figure 5B**).
268 We then incubated the recombinant KMN network immobilized on anti-Flag M2 beads with
269 bacterially expressed Ipl1/6xHis-Sli15 (**Figure 5C**). Western blotting indicated that our
270 Ipl1/6xHis-Sli15 preparation contained two major forms of Sli15, both recognized by the anti-
271 His antibody. The faster migrating form is therefore a C-terminal truncation of Sli15. We found
272 that wildtype Kre28 and Kre28$^{\Delta Zwint}$ KMN networks, but not empty control beads, bound the
273 Ipl1/Sli15 complex in the pull down experiment, with the full length Sli15 form being detected
274 preferentially in the pull down (**Figure 5C**). Whereas Ipl1/Sli15 appeared to bind equally well
275 to both wildtype and mutant KMN networks, the association of Mtw1c/Ndc80c to Spc105/Kre28
276 was slightly reduced in the Kre28$^{\Delta Zwint}$ mutant. Adjusting the pull down protocol to prolonged
277 incubation times, led to a more complete dissociation of Mtw1c/Ndc80c from Spc105/Kre28,
278 while Ipl1/Sli15 binding was largely preserved (**Figure EV3 A**). Kinase assays showed that
279 Spc105, Ndc80 and Dsn1 were major KMN substrates of Ipl1, as anticipated from previous
280 work (de Regt *et al*, 2022). Interestingly, Ipl1 autophosphorylation - a readout for its activity -
281 appeared to be increased in the presence of the KMN network (**Figure EV3 B,C**).
282 We next compared the ability of Ipl1/Sli15 to bind to the different subcomplexes of the KMN
283 network by immobilizing Spc105-Flag/Kre28 (K subcomplex) or Mtw1c/Ndc80c-Flag (MN
284 subcomplexes) separately on anti-Flag M2 beads. Western blotting showed that Ipl1/Sli15
285 interacted exclusively with Spc105/Kre28, but not with Ndc80c/Mtw1c under these conditions
286 (**Figure 5 D**).
287 Our initial characterization showed that the Ipl1/Sli15 complex was autophosphorylated
288 following expression and purification from *E. coli*. We tested the effect of Ipl1
289 autophosphorylation on the binding to immobilized Spc105/Kre28 by comparing an untreated
290 control with samples including either ATP (to promote phosphorylation) or Lambda
291 phosphatase (to eliminate phosphorylation). We found that inclusion of ATP strongly reduced
292 the association of Ipl1/Sli15 with Spc105/Kre28, while addition of Lambda phosphatase
293 promoted binding (**Figure 5E**). Judged by protein band intensity, near stoichiometric amounts
294 of Ipl1 seemed to bind to immobilized Spc105/Kre28 in the untreated or Lambda phosphatase-
295 treated sample. Thus, we conclude that Ipl1/Sli15 binds recombinant KMN *in vitro* via the
296 Spc105/Kre28 complex and that this interaction can be counteracted by Ipl1
297 autophosphorylation.
298 Unlike the checkpoint kinase Mps1, the Ipl1/Sli15 kinase complex is typically not recovered as

299 a stable component of kinetochore purifications from yeast extracts using Dsn1-Flag (Akiyoshi
300 *et al*, 2010). Using a proximity-dependent *in vivo*-biotinylation approach with the TurboID
301 Ligase (Fenech *et al*, 2023) we found, however, that Sli15-6xFlag could be detected in
302 Streptavidin affinity-purifications from extracts of strains that expressed Spc105-TurboID,
303 similar to the constitutive Spc105 binding partner Kre28 (**Figure 5F**). The nuclear kinesin-5
304 motor protein Cin8, expressed at a lower level and implicated in the regulation of kinetochores
305 via Ndc80 (Gardner *et al*, 2008; Suzuki *et al*, 2018), on the other hand, was not recovered with
306 Spc105-TurboID. This supports the idea that Spc105-Sli15 interactions also occur *in vivo*,
307 although possibly only transiently.
308

309 To characterize the KMN-Ipl1/Sli15 assembly in more detail, we conducted chemical
310 crosslinking with the homo-bifunctional amine-to-amine crosslinker BS3, followed by mass
311 spectrometry (XL-MS)(Herzog *et al*, 2012). The resulting Lys-Lys proximity map is in overall
312 agreement with the established KMN subunit topology (**Figure 6A and B**). In particular it
313 showed that the C-termini of the subunits Mtw1, Dsn1 and Nsl1 are closely connected to each
314 other and proximal to Spc105/Kre28 and to the Spc24/Spc25 heterodimer of the Ndc80
315 complex (Dimitrova *et al.*, 2016; Ghodgaonkar-Steger *et al.*, 2020; Malvezzi *et al.*, 2013). The
316 majority of Sli15/Ipl1 crosslinks to the KMN network is found on the Spc105-Kre28 subcomplex
317 (17 different crosslinks to Spc105/Kre28, 4 to Mtw1c and 4 to Ndc80c). In particular, the
318 Spc105 segment 450-700, encompassing the helix bundle with Kre28, is found in proximity to
319 Sli15. On Sli15 most crosslinks are found between residues 200 and 250, marking the
320 transition between the amino-terminal CEN localization module and the central phospho-
321 regulated (PR) domain, previously implicated in microtubule-binding. For instance, Sli15 K217
322 displays crosslinks to Spc105 K527 and K607, both located in the helix bundle domain. Overall,
323 these crosslinks are consistent with the binding experiments, showing that Spc105/Kre28 is
324 the main interaction partner of Ipl1/Sli15 in the outer kinetochore KMN network.

325
326

327 **Binding of a Sli15 segment to the Spc105/Kre28 helix bundle is essential for**
328 **chromosome segregation in cells**

329 Guided by the crosslinking results we performed AlphaFold structure predictions with N-
330 terminal Sli15 segments of varying length. Strikingly, Sli15 segment 215-255 yielded a high
331 confidence model on the Spc105/Kre28 helix bundle (pTM and ipTM scores >0.85) (**Figure 7A,**
332 **Figure EV4A and B**). The predicted binding mode includes a short alpha-helix at the N-
333 terminus of the Sli15 peptide (residues 224-236) and an extended segment that binds across

334 the surface of the helix bundle (**Figure 7A**). The confidence of the prediction is highest in the
335 extended segment (236-248), while the alpha-helix shows some positional variance between
336 models (**Figure EV4B**). The Kre28 Zwint helix contributes only its C-terminus to the predicted
337 binding interface, the segment which also yielded the most severe phenotypes in our
338 mutational analysis (**Figure EV4C, Figure EV1**). The Sli15 arginine pair R231 and R232 is
339 predicted to form ionic interactions with Spc105 E510 and Spc105 E596. The Sli15 residue
340 L239 is buried in a hydrophobic pocket formed by Spc105 residues W579, W582 and L519,
341 and Sli15 K242 interacts with an acidic pocket formed by Spc105 E578, Kre28 E103 and Kre28
342 D106 (**Figure 7B**). The crucial residues are part of a conserved segment among yeast Sli15
343 proteins (**Figure 7C**). We generated a *sli15*^{4E} mutant exchanging these residues. An in vitro
344 pull down experiment showed reduced binding of Ipl1/6xHis-Sli15^{4E} to immobilized Spc105-
345 Kre28 (**Figure 7D**). We next replaced one copy of *SLI15* with Flag-tagged wildtype or *sli15*^{4E}
346 in diploid yeast cells. We constructed the 4E mutation in full-length Sli15 and in the Sli15$^{\Delta N}$
347 variant lacking the CEN localization module. Upon sporulation and dissection we failed to
348 recover viable *sli15*^{4E} mutant spores, both in full-length and in ΔN form (**Figure 7E**). This
349 indicates that *sli15*^{4E} is a lethal mutation, despite the mutant protein being expressed at the
350 same level as wildtype in the diploid (**Appendix Figure S3A, B**). Confirming this result, *sli15*^{4E}
351 also failed to rescue the acute depletion of *sli15-aid* in haploid yeast strains using an auxin-
352 dependent degron system (**Figure EV5A-C**). Dissecting the contributions of individual
353 residues in the auxin-degron system showed that *sli15*$^{R231E\ R232E}$ was viable, but benomyl-
354 hypersensitive, while *sli15*^{K242E} displayed a severe growth defect, similar to the 4E mutant
355 (**Figure EV5D**). The AlphaFold model also predicts that corresponding mutations in Spc105
356 should yield similar growth phenotypes. Consistent with this notion, the charge-reversing
357 mutations *spc105*$^{E578K\ E596K}$ displayed benomyl hypersensitivity and *spc105*$^{E510K\ E578K\ E596K}$ had
358 a severe growth defect in a conditional Spc105-FRB anchor-away system (**Figure EV5E, F**).

359 To analyze differences between wildtype and mutant *sli15*^{4E} in cells, we imaged mNeonGreen-
360 tagged variants in diploid yeast cells together with a kinetochore marker (Mtw1-mCherry).
361 While we did not observe significant localization differences between the full-length Sli15
362 versions, we noticed that *sli15*$^{\Delta N}$, unlike the full-length protein, localized very prominently to
363 the ends of anaphase spindles, displaying enrichment and precise overlap with the kinetochore
364 marker Mtw1 (**Figure 7F**). Importantly, the fraction of anaphase spindles showing co-
365 enrichment of Mtw1 and *sli15*$^{\Delta N,4E}$ was significantly reduced (**Figure 7G**). The 4E mutation did
366 not affect the overall spindle association and the difference to wildtype was most notable on
367 anaphase kinetochores. We conclude that the 4E mutation impairs Sli15 binding to a subset
368 of kinetochores in cells, a defect that is revealed when the CEN-localization module of Sli15 is
369 absent.

370

371 **Discussion**

372 **New *kre28* mutant alleles reveal specific contributions to outer kinetochore function**

373 While the molecular roles of Ndc80c and Mtw1c complexes in the kinetochore architecture are
374 well established, the functional contributions of Spc105/Kre28 still await further definition. The
375 mitotic checkpoint function of Spc105 is well understood, but it cannot account for its essential
376 role in budding yeast. The *kre28*$^{\Delta Zwint}$ allele described in this study can be used to reveal
377 additional aspects of Spc105/Kre28 function. We show that one of its effects is a selective
378 reduction of Spc105/Kre28 at the kinetochore without affecting the levels of Ndc80 and Mtw1
379 complexes. It is therefore much more selective than more penetrant perturbations. For
380 example, a depletion or reduction of human Knl1 by RNAi strongly affects the levels of
381 additional outer kinetochore components such as Ndc80/Hec1 as well (Caldas *et al*, 2013;
382 Desai *et al*, 2003), making it difficult to delineate a specific function. We note that the observed
383 Spc105/Kre28 reduction in metaphase cells is moderate and does not lead to impaired spindle
384 assembly checkpoint activity, as the mutant cells are fully capable of arresting in nocodazole.
385 In addition, they show normal levels of Sgo1 recruitment to the kinetochore in prometaphase,
386 suggesting sufficient Bub1 activity at the kinetochore. We currently cannot provide a precise
387 molecular explanation for why the mutations in the Kre28 helical bundle may reduce the affinity
388 of Spc105/Kre28 for Ndc80c/Mtw1c, both *in vivo* and *in vitro*. Even though AlphaFold2 models
389 predict multiple possible conformations of KMN, they do not show a binding interface within
390 KMN that would include the Kre28 Zwint helix. It is also possible that diminished kinetochore
391 recruitment may be a consequence of the reduced Ipl1 activity in the mutant. Future
392 experiments will have to clarify this point using some of the more specific mutations discovered
393 in our study.

394

395 **An outer kinetochore recruitment mechanism for the Ipl1/Sli15 kinase complex**

396 Taken together, the following lines of evidence support the conclusion that the *kre28* helical
397 bundle mutant phenotype is caused by insufficient or misregulated Ipl1 activity at the outer
398 kinetochore.

399 1. The phenotypes of the *kre28*$^{\Delta Zwint}$ mutant strongly resemble defects in the tension-dependent
400 error correction pathway. The mutant cells have a functional mitotic checkpoint in response to
401 nocodazole, but when forced to reassemble a spindle following nocodazole withdrawal, they
402 ignore biorientation problems and missegregate chromosomes without delaying the initiation
403 of anaphase. The lack of a delay indicates that the cells can form kinetochore-microtubule
404 attachments, because otherwise the unattached kinetochores would activate the checkpoint.

405 This characteristic behavior is also displayed by *sgo1* mutants (Indjeian *et al.*, 2005) and
406 indicates an inability to sense the incorrect attachment status.
407 2. The genetic interaction profile indicates that the *kre28* mutant is very sensitive to further
408 perturbations of Ipl1/Sli15, its recruitment pathways, or mutations in its outer kinetochore
409 substrates.
410 3. The *kre28*$^{\Delta Zwint}$ mutant is suppressed by artificial recruitment of Ipl1 via an Mtw1-Sli15 fusion
411 protein. We show that the Mtw1-Sli15 fusion can only suppress the phenotype when capable
412 of binding Ipl1. The observed rescue is only partial, partly due to the fact the fusion protein is
413 expressed over a wildtype Mtw1 and therefore will have to compete with it for kinetochore
414 incorporation. The fusion is also constitutive, preventing a dynamic regulation of Ipl1
415 recruitment that may occur in wildtype cells. We nevertheless suspect that fusing the Sli15
416 segment to the C-terminus of Mtw1 reintroduces Ipl1 at a compatible location within KMN,
417 while previous studies have reported constitutive Sli15 fusions to Ndc80 to be incompatible
418 with biorientation (Li *et al*, 2023). Our live cell imaging experiment using fluorescently labelled
419 chromosomes demonstrates that an improved chromosome segregation after nocodazole
420 washout is the basis for the suppression of the growth defect.
421 4. Recombinant Ipl1/Sli15 binds KMN via the Spc105/Kre28 subunits *in vitro*. The chemical
422 crosslinking-mass spectrometry experiments are consistent with Spc105/Kre28 providing the
423 main binding site within the KMN network. Autophosphorylation of Ipl1/Sli15 inhibits binding,
424 possibly preventing excessive Ipl1/Sli15 recruitment, which would hinder the re-establishment
425 of kinetochore-microtubule attachments during error correction. Also phosphorylation of
426 Spc105/Kre28 may contribute to regulatory mechanisms, this point will need to be dissected
427 in futures studies. Our findings are consistent with earlier reports showing that depletion of
428 Knl1 appears to reduce Aurora B substrate phosphorylation in human cells (Caldas *et al.*,
429 2013).
430 5. A Sli15 peptide motif in the central domain is predicted with high confidence to bind the
431 Spc105/Kre28 helical bundle. AlphaFold-guided mutations in Sli15 or corresponding mutations
432 in Spc105/Kre28 are lethal or have severe growth defects, consistent with fatal problems in
433 chromosome segregation.
434
435
436 **Implications for the tension-sensing mechanism of the kinetochore**
437 Our results re-affirm the notion that Bir1/Nbl1-based CEN recruitment of the CPC is not
438 required for chromosome bi-orientation in yeast cells (**Figure 8A**). Previously, this has been
439 attributed to enhanced clustering of the Sli15$^{\Delta N}$ complex on microtubules (Campbell & Desai,
440 2013). Our results allow a more straightforward explanation: The Sli15$^{\Delta N}$ complex contains
441 crucial outer kinetochore binding sites that are sufficient to provide full functionality during

chromosome bi-orientation. We show that a segment in the Sli15 central domain binds to the Spc105/Kre28 helix bundle. Mutational analysis indicates that this binding interface is a key element in the tension-dependent error correction mechanism. Crucially, the *sli15*^{4E} mutant does not only cause a growth phenotype in the *sli15*$^{\Delta N}$ version, but also in the full-length protein. Binding of Sli15 to Spc105/Kre28 is therefore not just a backup mechanism that only becomes important when the regular CEN-based localization is absent, but it must be an important element of the tension sensing and signaling mechanism in general. The lethality of the *sli15*^{4E} point mutant implies that tension-sensing must occur in the outer kinetochore KMN architecture. Defining the terminal phenotype of the *sli15*^{4E} mutant more precisely, will be an important point in future studies.

Previous models have emphasized the role of CPC centromere-anchoring in separating the kinase from its substrates under tension (Liu *et al*, 2009). Sli15^{INCENP} performs a key function as it can restrict the reach of the kinase in the kinetochore (Krenn & Musacchio, 2015). Our results reveal that Sli15 needs to be connected to very specific points within the KMN architecture in order to measure intra-kinetochore tension (**Figure 8B**). Notably, movements of the K-arm (including Spc105/Kre28) relative to other parts of the kinetochore have been documented (Wan *et al*, 2009). The Ipl1/Sli15 kinase module of the CPC is therefore an integral part of the outer kinetochore and can be influenced by architectural and conformational changes that occur in different attachment situations. Future experiments will have to fully define the underlying outer kinetochore binding mechanism and ask how the Ipl1 kinase activity towards key substrates may be influenced by distinct KMN conformations under force.

466 ## Methods

467 **Cultivation and genetic manipulation of yeast**

468 All yeast strains used in this study are based on the S288C strain. Standard techniques were
469 used for cultivation and genetic manipulation of yeast strains. PCR-generated integration
470 cassettes were generated as described in Longtine *et al*, 1998 and Janke *et al*, 2004.
471 Alternatively, linearized plasmids with ends homologous to the site of integration were used for
472 transformation. Plasmids used for yeast transformation are listed in the reagents and tools
473 table, a full list of yeast strains it provided in Appendix Table S1.
474

475 **Sporulation and dissection of diploid yeast strains**

476 Cells from 1 ml of a saturated overnight culture of diploid yeasts strains were washed twice
477 with 1 ml ddH_2O, resuspended in 4 ml sporulation medium and incubated at room temperature
478 for several days until tetrads were formed. 250 µl of the sporulation culture were centrifuged
479 and the cell pellet was resuspended in 37.5 µl Zymolase T (1 mg/ml) and incubated at 37 °C
480 for 3.5 minutes. Afterwards, 200 µl of cold 100 mM potassium phosphate buffer (pH 7.0) was
481 added. A few microliters of the cell suspension were streaked out on a YEPD plate and tetrads
482 were dissected using a Singer MSM semi-automated dissecting microscope. Plates were
483 incubated at 30 °C for three days. For genotyping, the spores were resuspended in minimal
484 medium and spotted on YEPD, drop-out and mating type tester plates.
485

486 **Serial dilution assay**

487 Cells from a saturated overnight culture were diluted to OD_{600} = 0.4 in minimal medium and
488 serially diluted (1:4, six dilution steps in total). Cells were spotted on YEPD or YEPD + benomyl
489 (20 µg/ml; Sigma-Aldrich) plates using a pinning tool. Plates were incubated at 25 °C, 30 °C
490 or 37 °C for two days or at 16 °C for five days.
491

492 **Preparation of western blot samples from yeast cultures**

493 Samples for western blot analysis were prepared according to a protocol adapted from
494 (Kushnirov, 2000). In brief, an equivalent of 2 OD_{600} from a logarithmically growing culture was
495 harvested by centrifugation, resuspended in 100 µl ddH_2O and 100 µl 0.2 M NaOH was added.
496 Samples were incubated at room temperature for five minutes, cells were pelleted,
497 resuspended in 50 µl SDS-PAGE loading buffer and boiled at 95 °C for five minutes. 6 – 8 µl
498 of sample were loaded for SDS-PAGE. Proteins were transferred to a Amersham™ Protran™
499 Nitrocellulose Blotting Membrane (Cytiva) by wet transfer. Membranes were blocked in TBST
500 with 5 % (w/v) skimmed milk, incubated with the respective antibodies (listed in R&T table)

501 and membranes were washed in TBST. For detection of signals from HRP-conjugated
502 antibodies, membranes were incubated with ECL™ (Prime) Western Blotting Detection
503 Reagents (Cytiva). Signals were visualized using an Amersham Imager 600 (GE Healthcare).
504
505
506

507 **Analysis of cell cycle progression after release from α factor arrest into medium with**
508 **nocodazole**

509 Cells from a saturated overnight culture were diluted to OD_{600} = 0.2 and incubated at 30 °C
510 from 1 hour. α factor was added to a final concentration of 10 µg/ml and cells were further
511 incubated at 30 °C for 2 – 2.5 hours. Arrest in G1 phase was confirmed by microscopy when
512 more than 90 % of cells had a shmoo. Cells were subsequently collected by centrifugation,
513 washed two times with pre-warmed YEPD supplemented with 100 µg/ml pronase (Roche) and
514 once with pre-warmed YEPD without pronase. Cells were resuspended in pre-warmed YEPD
515 with 15 µg/ml nocodazole (Sigma) and further cultivated at 30 °C. Samples for western blot
516 analysis were taken immediately and every 30 minutes after release from the α factor arrest.
517
518

519 **Analysis of cell cycle progression after release from a nocodazole arrest**

520 Cells from a saturated overnight culture were diluted to OD_{600} = 0.2 and grown at 30 °C for
521 1.5 hours. Nocodazole was added to a final concentration of 15 µg/ml, followed by further
522 incubation at 30 °C for 2 hours. Arrest in mitosis was confirmed by microscopy when more than
523 90 % of cells were large budded. Cells were harvested by centrifugation, washed three time
524 with pre-warmed YEPD, resuspended in pre-warmed YEPD with 10 µg/ml α factor to arrest
525 cells in the next G1 phase and further cultivated at 30 °C. Samples for western blot analysis
526 were collect every 15 minutes after release from the nocodazole arrest.
527

528 **Viability assay after nocodazole treatment**

529 Cells from a saturated overnight culture were diluted to OD_{600} = 0.2 and incubated at 30 °C for
530 3 hours. Nocodazole was added to a final concentration of 15 µg/ml and cultures were further
531 incubated at 30 °C for 1.5 hours. Before and after nocodazole treatment, an aliquot was taken
532 from the cultures and serially diluted to OD_{600} = 0.0004. 100 µl of the diluted culture were plated
533 on YEPD plates and incubated at 30 °C for two days. The number of colonies grown on each
534 plate was counted. For each strain, the number of colonies formed in the untreated sample

535 was defined as 100 %.
536

537 **Live cell microscopy**

538 For live cell microscopy to quantify fluorescence signal intensities, cells from a saturated
539 overnight culture were diluted to OD_{600} = 0.2 in YEPD medium and grown at 30 °C for four to
540 five hours. Cells were then immobilized on glass bottom dishes (No 1.5, MatTek corporation)
541 coated with 0.1 mg/ml concanavalin A (Sigma) and the dish was filled with SD doTrp medium.
542 To analyze chromosome segregation after nocodazole washout, cells were diluted to
543 OD_{600} = 0.2 in YEPD medium and grown at 30 °C for two hours. Cells were treated with
544 15 µg/ml nocodazole, further incubated at 30 °C for 1.5 hours and then immobilized in multi
545 well glass bottom dishes (Ibidi) coated with 0.1 mg/ml concanavalin A (Sigma). The Cells were
546 washed three times with SD doTrp to wash out the nocodazole and the imaging chamber was
547 filled with SD doTrp. Images were acquired at 10 minutes intervals over a total time of 1.5 to
548 2 hours. All media were supplemented with 100 µM $CuSO_4$ to induce expression of LacI-GFP
549 which is under control of the Cup1 promoter.
550 All microscopy was performed with a DeltaVision Elite wide-filed microscope (GE Healthcare
551 Life Sciences) with a Super-Plan Apo 100x/1.4 oil objective, solid state light source (SSCI) and
552 sCMOS camera. Imaging was performed at 30 °C. Z-stacks with a spacing of 0.4 µm covering
553 a total distance of 6 µm were acquired and maximum projections were generated. Alternatively,
554 OAI (optical axis integration) scans over 6 µm were performed. Images were deconvolved
555 using the default settings of the SoftWoRx software (GE Healthcare Life Sciences).
556

557 **Quantification of fluorescence microscopy**

558 Fluorescence microscopy signals were quantified using Fiji. Equally sized boxes were drawn
559 around individual kinetochore clusters of metaphase or anaphase cells and the mean
560 integrated density was measured. Additionally, the local background in proximity to the
561 kinetochore cluster was measured and subtracted from the signal.
562 For each experimental data set, the mean value measured for metaphase kinetochore clusters
563 of the $Kre28^{WT}$ strain was defined as 1.0 as and all other data was normalized accordingly for
564 better comparison.
565 To quantify the fraction of anaphase spindles showing kinetochore proximal Sli15-
566 mNeonGreen foci (Figure 7 F-G), the projected images were blinded and randomized. From
567 these images, the anaphases were classified based on the distribution of Sli15-mNeonGreen
568 along the spindle.

569

570 **Statistical analysis**

571 Data was analyzed and visualized using the statistics software GraphPad Prism 10. Mean
572 values +/- standard deviation (SD) are displayed. Information on sample size and applied
573 statistical tests are provided in the figure legends.

574

575 **Multiple sequence alignments and secondary structure prediction**

576 Multiple sequence alignments were performed with sequences of Kre28 proteins from different
577 yeast species or with sequences of Kre28 and Zwint related proteins from various eukaryotic
578 species were used.

579 Sequences from yeast species were aligned using the MAFFT multiple alignment tool (Katoh
580 *et al*, 2019). Alignments were visualized in Jalview (Waterhouse *et al*, 2009) with Clustal
581 coloring and 50 % conservation threshold.

582 Secondary structure predictions of *S. cerevisiae* Kre28 and *H. sapiens* Zwint were generated
583 using the JPred4 server (Drozdetskiy *et al*, 2015).

584

585 **ColabFold structure predictions**

586 The structure of the Spc105$^{490-917}$/Kre28 heterodimer in Figure 1A was predicted using
587 Colabfold
588 (https://colab.research.google.com/github/sokrypton/ColabFold/blob/main/beta/AlphaFold2_a
589 dvanced.ipynb)(Mirdita *et al*, 2022) with the following parameters: msa_method=mmseqs2,
590 pair_mode=unpaired, cov=0, qid=0, max_msa=512:1024, subsample_msa=True,
591 num_relax=0, use_turbo=True, use_ptm=True, rank_by=pLDDT, num_models=5,
592 num_samples=1, num_ensemble=1, max_recycles=3, tol=0, is_training=False,
593 use_templates=False. The figures of the predicted structures were further processed using the
594 software ChimeraX (Pettersen *et al*, 2004). pLDDT values were colored in ChimeraX.
595 Visualization of the predicted alignment errors was prepared by Colabfold.

596

597 **AlphaFold2 molecular modelling**

598 AlphaFold (AF) was used for all molecular modeling in the versions AF2 Multimer 3.2.1
599 (preprint:Evans *et al*, 2022) and AF3 (Abramson *et al*, 2024). A general feature of AF2 Multimer
600 is the higher sensitivity to intra- and intermolecular interactions compared to the original AF2
601 (Jumper *et al*, 2021). For the model shown in Fig. 7A, B the input sequences *S.cerevisiae*
602 Spc105_449-642 (P53148); Kre28_1-208 (Q04431) and Sli15_215-255 (P38283) were used.
603 PAE-scores for this interface were consistently >0.8 and AF2 and AF3 yielded very similar
604 predictions. Segment Sli15 236-248 was predicted with the highest confidence, the Sli15 alpha
605 helix 224-236 scored slightly lower in pLDDT. The point mutations Sli15 R231E R232E L239E

606 K242E, were designed based on the AF2 prediction using manual inspection as well as a PISA
607 analysis (Krissinel & Henrick, 2007).
608

609 **Expression of recombinant proteins in *Sf9* insect cells**

610 KMN and individual KMN subcomplexes were expressed in Sf9 (*Spodoptera frugiperda*) insect
611 cells. Cells were infected with baculoviruses carrying expression constructs for the respective
612 protein complexes. Information about baculoviruses used in this study are listed in the R&T
613 table. For expression of the ten subunit KMN network, cells were co-infected with KT1-5 and
614 KT1-6. Sf9 cells were split to a cell density of 0.8 x 10^6 cells/ml and grown at 27 °C with gentle
615 agitation. Next day, cells were infected with the respective baculoviruses and harvested two to
616 three days after infection.
617

618 **Pull down assays**

619 For pull down assays using proteins expressed in Sf9 cells, cells were resuspended in
620 interaction buffer (25 mM HEPES pH 7.4, 200 mM NaCl, 1 mM $MgCl_2$, 2.5 % (v/v) glycerol,
621 0.01 % (v/v) Tween-20) supplemented with 1 mM PMSF and Pierce™ Protease Inhibitor
622 (EDTA-free; ThermoFisher Scientific) and lysed by sonication. Lysates were cleared by
623 centrifugation. Anti-Flag M2 agarose beads (Sigma-Aldrich) were preequilibrated with
624 interaction buffer and incubated with the cleared lysate overnight, rotating at 4 °C. Afterwards,
625 beads were washed three times for 5 minutes with interaction buffer and loaded beads were
626 split into individual pull down samples.
627 To test for binding of Ipl1/Sli15 or Ipl1 to KMN or individual subcomplexes, 100 µl of 2 µM
628 Ipl1/Sli15 or Ipl1 was added to approximately 20 µl of loaded beads. As controls, Ipl1/Sli15 or
629 Ipl1 was also added to unloaded beads or loaded beads were incubated with interaction buffer
630 without any protein. 20 µl of the assembled reactions was taken as input samples for SDS-
631 PAGE analysis. Pull down samples were subsequently incubated rotating at 4 °C for 6 h.
632 Afterwards, beads were collected by centrifugation, the supernatant was removed, and the
633 beads were washed three times with 200 µl interaction buffer. Proteins bound to the beads
634 were eluted by addition of 50 µl interaction buffer with 0.5 or 1.0 µg/µl 3xFlag peptide, followed
635 by incubation at 4 °C for one to two hours.
636

637 ***In vitro* KMN stability assay**

638 Sf9 cells expressing KMN with either $Kre28^{WT}$ or $Kre28^{\Delta Zwint}$ were resuspended in interaction
639 buffer (25 mM HEPES pH 7.4, 200 mM NaCl, 1 mM $MgCl_2$, 2.5 % (v/v) glycerol, 0.01 % (v/v)
640 Tween-20) supplemented with 1 mM PMSF and Pierce™ Protease Inhibitor (EDTA-free;
641 ThermoFisher Scientific) and lysed by sonication. Lysates were cleared by centrifugation,

642 added to M2 anti-Flag agarose beads (Sigma-Aldrich) preequilibrated with interaction buffer
643 and incubated overnight rotating at 4 °C. Next day, beads were washed three times for five
644 minutes with 1 ml interaction buffer and 730 µl interaction buffer was added to the beads.
645 Samples were collected immediately and 3, 6 and 24 hours after addition of the buffer. Beads
646 were collected by centrifugation and once briefly washed with 200 µl of interaction buffer. 50 µl
647 of interaction buffer with 1 µg/µl 3xFlag peptide was added to the beads and samples were
648 incubated rotating at 4 °C for 1.5 hours to elute proteins from the beads. Samples were
649 subsequently analyzed by SDS-PAGE and Coomassie staining.
650

651 ***In vitro* phosphorylation and dephosphorylation of Ipl1/Sli15**

652 Recombinant Ipl1/Sli15 was diluted in interaction buffer (25 mM HEPES pH 7.4, 200 mM NaCl,
653 1 mM $MgCl_2$, 2.5 % (v/v) glycerol, 0.01 % (v/v) Tween-20) supplemented with 1 mM $MnCl_2$. λ-
654 Protein Phosphatase (NEB) or 500 µM ATP was added and samples were incubated at 30 °C
655 for 30 minutes.
656

657 ***In vitro* kinase assay**

658 *In vitro* kinase reactions were prepared in a total reaction volume of 90 µl. Recombinant KMN,
659 Ipl1/Sli15 or a mixture of KMN and Ipl1/Sli15 were diluted in kinase buffer (20 mM HEPES
660 pH 7.4, 100 mM KCl, 10 mM $MgCl_2$, 10 mM $MnCl_2$, 25 mM β-glycerol phosphate, 1 mM DTT)
661 supplemented with 100 µM cold ATP and 83.25 nM hot ^{32}P-γ-ATP (Hartmann Analytic).
662 Samples were incubated at 30 °C and 20 µl aliquots were taken after 0, 5, 15 and 30 minutes.
663 Reactions were stopped by addition of 6x SDS-PAGE loading buffer, boiled at 95 °C and
664 analyzed by SDS-PAGE. Gels were stained with Coomassie dried afterwards. ^{32}P
665 autoradiography was detected with a FLA-3000 Imaging Scanner (Fujifilm).
666

667 **Purification of recombinant Ipl1/Sli15 from *E. coli***

668 Ipl1/6xHis-Sli15 (wildtype or 4E mutant) was expressed in BL21 *E. coli* cells. 4 L TB medium
669 with 50 µg/ml kanamycin were inoculated with 100 ml of a saturated overnight culture. Cells
670 were incubated at 37 °C, shaking at 180 rpm, until an $OD_{600} \approx 0.7$ was reached. Expression of
671 Ipl1/Sli15 was induced by addition of 0.4 mM IPTG. Cells were further incubated for 3 h and
672 afterwards harvested by centrifugation, washed in PBS and stored at -80 °C until further
673 processing.
674 Cells were resuspended in 90 ml lysis buffer (50 mM Na_2HPO_4/NaH_2PO_4 pH 8.0, 300 mM
675 NaCl, 5 % (v/v) glycerol, 20 mM imidazole, 0.5 mM TCEP) supplemented with Pierce™
676 Protease Inhibitor (EDTA-free; ThermoFisher Scientific) and 1 mM PMSF and lysed by
677 sonication. The lysate was cleared by centrifugation and loaded onto two serially connected

678 HisTrap 5 ml columns (Cytiva) which were connected to a ÄKTA FPLC system (GE
679 Healthcare). Columns were washed with lysis buffer and bound proteins were eluted with a
680 linear imidazole gradient (20 – 500 mM). Elution fractions were collected and analyzed by
681 SDS-PAGE. Fractions of comparable quality were pooled, concentrated to approximately
682 500 µl and subjected to size exclusion chromatography using Superdex 200 10/300 GL
683 column (GE Healthcare; 20 mM HEPES pH 7.4, 250 mM NaCl, 1 mM $MgCl_2$, 5 % (v/v)
684 glycerol, 0.5 mM TCEP). Elution fractions were analyzed by SDS-PAGE and comparable
685 samples were pooled, aliquoted, snap-frozen in liquid N_2 and stored at -80 °C.
686

687 **In vivo biotinylation and affinity purification with TurboID**

688 Cell extracts from the respective yeast strains were prepared from log-phase cultures. Cells
689 were lysed by bead-beating (BioSpec) in Lysis buffer (20 mM Hepes pH 7.4, 200 mM NaCl,
690 1 mM $MgCl_2$, 0.5 mM TCEP, 2.5 % glycerol. After centrifugation, 500 µl cleared lysate was
691 incubated with 50 µl pre-equilibrated streptavidin-sepharose beads (Cytiva) with rotation at
692 4°C overnight. Beads were washed twice with wash buffer (Lysis buffer + 0.05 % (v/v) TX-100),
693 twice with wash buffer + 2 % (w/v) SDS, twice with wash buffer + 0.1 % (w/v) SDS and finally
694 twice with wash buffer. Proteins were eluted off the beads with SDS-PAGE loading buffer and
695 analyzed by western blotting.
696

697 **Pt/C low angle rotary shadowing electron microscopy**

698 The peak elution fractions from gel filtrations of recombinant KMN complexes were further
699 prepared for rotary shadowing EM analysis by diluting the complexes to ~70 µg/ml in spraying
700 buffer, containing 100 mM ammonium acetate and 30 % (v/v) glycerol, pH adjusted to 7.4. After
701 dilution, the samples were sprayed onto freshly cleaved mica chips and immediately
702 transferred into a Bal-Tec MED020 high vacuum evaporator equipped with electron guns. After
703 drying in the vacuum, the rotating samples were coated with 0.5 nm platinum at an elevation
704 angle between 5° and 6°, followed by 7 nm carbon at 90°. The produced replicas were floated
705 off from the mica chips and picked up on 400mesh Cu/Pd grids. The grids were inspected in
706 an FEI Morgagni 268D TEM operated at 80kV. Electron micrographs were acquired using an
707 11 megapixel Morada CCD camera from Olympus-SIS. Fiji was used for image analysis.
708

709 **Chemical crosslinking and mass spectrometry**

710 50-60 µg of recombinant protein complexes were crosslinked with 1:1 isotopically-labeled
711 (d_0/d_{12}) BS3 (Bis[sulfosuccinimidyl] suberate, Creative molecules) in a Thermomixer at 35°C
712 for 30 min at 1200 rpm. The reaction was quenched with 100 mM ammonium bicarbonate for
713 5 minutes at room temperature and supplemented with 8 M urea to a final concentration of

714 6 M. After reduction and alkylation crosslinked proteins were digested with Lys-C (1:50 w/w,
715 Wako) for 3 hours, diluted with 50 mM ammonium bicarbonate to 1 M urea and digested with
716 trypsin (1:50 w/w, Promega) overnight. Crosslinked peptides were purified by reversed phase
717 chromatography using C18 cartridges (Sep-Pak, Waters). Crosslinked peptides were enriched
718 by peptide size exclusion chromatography and analyzed by tandem mass spectrometry
719 (Orbitrap Elite, Thermo Scientific). Fragment ion spectra were searched and crosslinks
720 identified by the dedicated software program xQuest (Walzthoeni *et al*, 2012).

721

722 **Data availability**

723 The mass spectrometry proteomics chemical crosslinking data have been deposited to the
724 ProteomeXchange Consortium via the PRIDE (Perez-Riverol *et al*, 2022) partner repository
725 with the dataset identifier PXD059609. Link: https://www.ebi.ac.uk/pride/login, Project
726 accession PXD059609, Token: MbN7nK23eYD8

727

728 **Expanded View** for this article is available online.

729

730 **Acknowledgements**

731 This work was funded by the Deutsche Forschungsgemeinschaft (DFG, German Research
732 Foundation) – SFB1430 – Project-ID 424228829. Microscopy experiments were carried out
733 with support from the Imaging Center Campus Essen Core Facility (ICCE). The DeltaVision
734 Elite high resolution microscope was obtained through Deutsche Forschungsgemeinschaft
735 funding (Major Research Instrumentation Program as per Art. 91b GG, INST 20876/275-1).
736 The laboratory of F.H. was supported by the European Research Council (ERC)-StG (638218)
737 and by the GFF NÖ (Endowed Professorship, Province of Lower Austria).

738

739 **Disclosure and Competing Interests Statement**

740 The authors declare no competing interests.

741

742

743

744

References

Abramson J, Adler J, Dunger J, Evans R, Green T, Pritzel A, Ronneberger O, Willmore L, Ballard AJ, Bambrick J *et al* (2024) Accurate structure prediction of biomolecular interactions with AlphaFold 3. *Nature* 630: 493-500

Akiyoshi B, Sarangapani KK, Powers AF, Nelson CR, Reichow SL, Arellano-Santoyo H, Gonen T, Ranish JA, Asbury CL, Biggins S (2010) Tension directly stabilizes reconstituted kinetochore-microtubule attachments. *Nature* 468: 576-579

Biggins S, Murray AW (2001) The budding yeast protein kinase Ipl1/Aurora allows the absence of tension to activate the spindle checkpoint. *Genes Dev* 15: 3118-3129

Broad AJ, DeLuca KF, DeLuca JG (2020) Aurora B kinase is recruited to multiple discrete kinetochore and centromere regions in human cells. *Journal of Cell Biology* 219: e201905144

Caldas GV, DeLuca KF, DeLuca JG (2013) KNL1 facilitates phosphorylation of outer kinetochore proteins by promoting Aurora B kinase activity. *J Cell Biol* 203: 957-969

Campbell CS, Desai A (2013) Tension sensing by Aurora B kinase is independent of survivin-based centromere localization. *Nature* 497: 118-121

Ciferri C, Pasqualato S, Screpanti E, Varetti G, Santaguida S, Dos Reis G, Maiolica A, Polka J, De Luca JG, De Wulf P *et al* (2008) Implications for Kinetochore-Microtubule Attachment from the Structure of an Engineered Ndc80 Complex. *Cell* 133: 427-439

de Regt AK, Clark CJ, Asbury CL, Biggins S (2022) Tension can directly suppress Aurora B kinase-triggered release of kinetochore-microtubule attachments. *Nature Communications* 13: 2152

Dendooven T, Zhang Z, Yang J, McLaughlin SH, Schwab J, Scheres SHW, Yatskevich S, Barford D (2023) Cryo-EM structure of the complete inner kinetochore of the budding yeast point centromere. *Science Advances* 9: eadg7480

Desai A, Rybina S, Müller-Reichert T, Shevchenko A, Shevchenko A, Hyman A, Oegema K (2003) KNL-1 directs assembly of the microtubule-binding interface of the kinetochore in C. elegans. *Genes Dev* 17: 2421-2435

Dimitrova YN, Jenni S, Valverde R, Khin Y, Harrison SC (2016) Structure of the MIND Complex Defines a Regulatory Focus for Yeast Kinetochore Assembly. *Cell* 167: 1014-1027 e1012

Drozdetskiy A, Cole C, Procter J, Barton GJ (2015) JPred4: a protein secondary structure prediction server. *Nucleic Acids Research* 43: W389-W394

Evans R, O'Neill M, Pritzel A, Antropova N, Senior A, Green T, Žídek A, Bates R, Blackwell S, Yim J *et al* (2022) Protein complex prediction with AlphaFold-Multimer. *bioRxiv*: 2021.2010.2004.463034

Fenech EJ, Cohen N, Kupervaser M, Gazi Z, Schuldiner M (2023) A toolbox for systematic discovery of stable and transient protein interactors in baker's yeast. *Molecular Systems Biology* 19: e11084

Fischbock-Halwachs J, Singh S, Potocnjak M, Hagemann G, Solis-Mezarino V, Woike S, Ghodgaonkar-Steger M, Weissmann F, Gallego LD, Rojas J *et al* (2019) The COMA complex interacts with Cse4 and positions Sli15/Ipl1 at the budding yeast inner kinetochore. *Elife* 8: e42879

García-Rodríguez LJ, Kasciukovic T, Denninger V, Tanaka TU (2019) Aurora B-INCENP Localization at Centromeres/Inner Kinetochores Is Required for Chromosome Bi-orientation in Budding Yeast. *Current Biology* 29: 1536-1544.e1534

Gardner MK, Bouck DC, Paliulis LV, Meehl JB, O'Toole ET, Haase J, Soubry A, Joglekar AP, Winey M, Salmon ED *et al* (2008) Chromosome congression by Kinesin-5 motor-mediated disassembly of longer kinetochore microtubules. *Cell* 135: 894-906

Ghodgaonkar-Steger M, Potocnjak M, Zimniak T, Fischbock-Halwachs J, Solis-Mezarino V, Singh S, Speljko T, Hagemann G, Drexler DJ, Witte G *et al* (2020) C-Terminal Motifs of the MTW1 Complex Cooperatively Stabilize Outer Kinetochore Assembly in Budding Yeast. *Cell Rep* 32: 108190

Hadders MA, Hindriksen S, Truong MA, Mhaskar AN, Wopken JP, Vromans MJM, Lens SMA (2020) Untangling the contribution of Haspin and Bub1 to Aurora B function during mitosis. *Journal of Cell Biology* 219: e201907087

Herzog F, Kahraman A, Boehringer D, Mak R, Bracher A, Walzthoeni T, Leitner A, Beck M, Hartl F-U, Ban N *et al* (2012) Structural probing of a protein phosphatase 2A network by chemical cross-linking and mass spectrometry. *Science (New York, NY)* 337: 1348-1352

Hindriksen S, Lens SMA, Hadders MA (2017) The Ins and Outs of Aurora B Inner Centromere Localization. *Frontiers in Cell and Developmental Biology* 5: 112

Hornung P, Troc P, Malvezzi F, Maier M, Demianova Z, Zimniak T, Litos G, Lampert F, Schleiffer A, Brunner M *et al* (2014) A cooperative mechanism drives budding yeast kinetochore assembly downstream of CENP-A. *Journal of Cell Biology* 206: 509-524

Indjeian VB, Stern BM, Murray AW (2005) The centromeric protein Sgo1 is required to sense lack of tension on mitotic chromosomes. *Science* 307: 130-133

Jeyaprakash AA, Klein UR, Lindner D, Ebert J, Nigg EA, Conti E (2007) Structure of a Survivin–Borealin–INCENP Core Complex Reveals How Chromosomal Passengers Travel Together. *Cell* 131: 271-285

Jumper J, Evans R, Pritzel A, Green T, Figurnov M, Ronneberger O, Tunyasuvunakool K, Bates R, Žídek A, Potapenko A *et al* (2021) Highly accurate protein structure prediction with AlphaFold. *Nature* 596: 583-589

Kato H, Jiang J, Zhou B-R, Rozendaal M, Feng H, Ghirlando R, Xiao TS, Straight AF, Bai Y (2013) A Conserved Mechanism for Centromeric Nucleosome Recognition by Centromere Protein CENP-C. *Science* 340: 1110-1113

Katoh K, Rozewicki J, Yamada KD (2019) MAFFT online service: multiple sequence alignment, interactive sequence choice and visualization. *Briefings in Bioinformatics* 20: 1160-1166

Krenn V, Musacchio A (2015) The Aurora B Kinase in Chromosome Bi-Orientation and Spindle Checkpoint Signaling. *Front Oncol* 5: 225

Krissinel E, Henrick K (2007) Inference of macromolecular assemblies from crystalline state. *J Mol Biol* 372: 774-797

Kushnirov VV (2000) Rapid and reliable protein extraction from yeast. *Yeast* 16: 857-860

Li S, Garcia-Rodriguez LJ, Tanaka TU (2023) Chromosome biorientation requires Aurora B's spatial separation from its outer kinetochore substrates, but not its turnover at kinetochores. *Current Biology* 33: 4557-4569

Liu D, Vader G, Vromans MJ, Lampson MA, Lens SM (2009) Sensing chromosome bi-orientation by spatial separation of aurora B kinase from kinetochore substrates. *Science* 323: 1350-1353

London N, Ceto S, Ranish JA, Biggins S (2012) Phosphoregulation of Spc105 by Mps1 and PP1 Regulates Bub1 Localization to Kinetochores. *Current Biology* 22: 900-906

Malvezzi F, Litos G, Schleiffer A, Heuck A, Mechtler K, Clausen T, Westermann S (2013) A structural basis for kinetochore recruitment of the Ndc80 complex via two distinct centromere receptors. *EMBO J* 32: 409-423

Meadows JC, Shepperd LA, Vanoosthuyse V, Lancaster TC, Sochaj AM, Buttrick GJ, Hardwick KG, Millar JBA (2011) Spindle Checkpoint Silencing Requires Association of PP1 to Both Spc7 and Kinesin-8 Motors. *Developmental Cell* 20: 739-750

Mirdita M, Schütze K, Moriwaki Y, Heo L, Ovchinnikov S, Steinegger M (2022) ColabFold: making protein folding accessible to all. *Nat Methods* 19: 679-682

Musacchio A, Desai A (2017) A Molecular View of Kinetochore Assembly and Function. *Biology (Basel)* 6: 5

Nijenhuis W, Vallardi G, Teixeira A, Kops GJPL, Saurin AT (2014) Negative feedback at kinetochores underlies a responsive spindle checkpoint signal. *Nature Cell Biology* 16: 1257-1264

Pagliuca C, Draviam VM, Marco E, Sorger PK, Wulf PD (2009) Roles for the Conserved Spc105p/Kre28p Complex in Kinetochore-Microtubule Binding and the Spindle Assembly Checkpoint. *PLOS ONE* 4: e7640

Parnell EJ, Jenson EE, Miller MP (2024) A conserved site on Ndc80 complex facilitates dynamic recruitment of Mps1 to yeast kinetochores to promote accurate chromosome segregation. *Curr Biol* 34: 2294-2307 e2294

Perez-Riverol Y, Bai J, Bandla C, Garcia-Seisdedos D, Hewapathirana S, Kamatchinathan S, Kundu DJ, Prakash A, Frericks-Zipper A, Eisenacher M *et al* (2022) The PRIDE database resources in 2022: a hub for mass spectrometry-based proteomics evidences. *Nucleic Acids Res* 50: D543-D552

Pesenti ME, Raisch T, Conti D, Walstein K, Hoffmann I, Vogt D, Prumbaum D, Vetter IR, Raunser S, Musacchio A (2022) Structure of the human inner kinetochore CCAN complex and its significance for human centromere organization. *Molecular Cell* 82: 2113-2131.e2118

Petrovic A, Keller J, Liu Y, Overlack K, John J, Dimitrova YN, Jenni S, van Gerwen S, Stege P, Wohlgemuth S *et al* (2016) Structure of the MIS12 Complex and Molecular Basis of Its Interaction with CENP-C at Human Kinetochores. *Cell* 167: 1028-1040.e1015

Petrovic A, Mosalaganti S, Keller J, Mattiuzzo M, Overlack K, Krenn V, De Antoni A, Wohlgemuth S, Cecatiello V, Pasqualato S *et al* (2014) Modular Assembly of RWD Domains on the Mis12 Complex Underlies Outer Kinetochore Organization. *Molecular Cell* 53: 591-605

Pettersen EF, Goddard TD, Huang CC, Couch GS, Greenblatt DM, Meng EC, Ferrin TE (2004) UCSF Chimera--a visualization system for exploratory research and analysis. *Journal of Computational Chemistry* 25: 1605-1612

Pleuger R, Cozma C, Hohoff S, Denkhaus C, Dudziak A, Kaschani F, Kaiser M, Musacchio A, Vetter IR, Westermann S (2024) Microtubule end-on attachment maturation regulates Mps1 association with its kinetochore receptor. *Curr Biol* 34: 2279-2293 e2276

Polley S, Raisch T, Ghetti S, Korner M, Terbeck M, Grater F, Raunser S, Aponte-Santamaria C, Vetter IR, Musacchio A (2024) Structure of the human KMN complex and implications for regulation of its assembly. *Nat Struct Mol Biol* 31: 861-873

Rosenberg JS, Cross FR, Funabiki H (2011) KNL1/Spc105 Recruits PP1 to Silence the Spindle Assembly Checkpoint. *Current Biology* 21: 942-947

Roy B, Sim J, Han SJY, Joglekar AP (2022) Kre28–Spc105 interaction is essential for Spc105 loading at the kinetochore. *Open Biology* 12: 210274

Schmitzberger F, Harrison SC (2012) RWD domain: a recurring module in kinetochore architecture shown by a Ctf19-Mcm21 complex structure. *EMBO Rep* 13: 216-222

Sessa F, Mapelli M, Ciferri C, Tarricone C, Areces LB, Schneider TR, Stukenberg PT, Musacchio A (2005) Mechanism of Aurora B Activation by INCENP and Inhibition by Hesperadin. *Molecular Cell* 18: 379-391

Shepperd LA, Meadows JC, Sochaj AM, Lancaster TC, Zou J, Buttrick GJ, Rappsilber J, Hardwick KG, Millar JBA (2012) Phosphodependent Recruitment of Bub1 and Bub3 to Spc7/KNL1 by Mph1 Kinase Maintains the Spindle Checkpoint. *Current Biology* 22: 891-899

Suzuki A, Gupta A, Long SK, Evans R, Badger BL, Salmon ED, Biggins S, Bloom K (2018) A Kinesin-5, Cin8, Recruits Protein Phosphatase 1 to Kinetochores and Regulates Chromosome Segregation. *Curr Biol* 28: 2697-2704 e2693

Tanaka TU, Zhang T (2022) SWAP, SWITCH, and STABILIZE: Mechanisms of Kinetochore–Microtubule Error Correction. *Cells* 11: 1462

Tromer EC, van Hooff JJE, Kops GJPL, Snel B (2019) Mosaic origin of the eukaryotic kinetochore. *Proceedings of the National Academy of Sciences* 116: 12873-12882

Walzthoeni T, Claassen M, Leitner A, Herzog F, Bohn S, Forster F, Beck M, Aebersold R (2012) False discovery rate estimation for cross-linked peptides identified by mass spectrometry. *Nat Methods* 9: 901-903

Wan X, O'Quinn RP, Pierce HL, Joglekar AP, Gall WE, DeLuca JG, Carroll CW, Liu S-T, Yen TJ, McEwen BF *et al* (2009) Protein Architecture of the Human Kinetochore Microtubule Attachment Site. *Cell* 137: 672-684

Waterhouse AM, Procter JB, Martin DMA, Clamp M, Barton GJ (2009) Jalview Version 2—a multiple sequence alignment editor and analysis workbench. *Bioinformatics* 25: 1189-1191

Wei RR, Al-Bassam J, Harrison SC (2007) The Ndc80/HEC1 complex is a contact point for kinetochore-microtubule attachment. *Nat Struct Mol Biol* 14: 54-59

Weir JR, Faesen AC, Klare K, Petrovic A, Basilico F, Fischböck J, Pentakota S, Keller J, Pesenti ME, Pan D *et al* (2016) Insights from biochemical reconstitution into the architecture of human kinetochores. *Nature* 537: 249-253

896 Wilson-Kubalek EM, Cheeseman IM, Yoshioka C, Desai A, Milligan RA (2008) Orientation and structure
897 of the Ndc80 complex on the microtubule lattice. *Journal of Cell Biology* 182: 1055-1061
898 Xiao H, Wang F, Wisniewski J, Shaytan AK, Ghirlando R, FitzGerald PC, Huang Y, Wei D, Li S, Landsman
899 D *et al* (2017) Molecular basis of CENP-C association with the CENP-A nucleosome at yeast
900 centromeres. *Genes Dev* 31: 1958-1972
901 Yamagishi Y, Yang C-H, Tanno Y, Watanabe Y (2012) MPS1/Mph1 phosphorylates the kinetochore
902 protein KNL1/Spc7 to recruit SAC components. *Nature Cell Biology* 14: 746-752
903 Yatskevich S, Muir KW, Bellini D, Zhang Z, Yang J, Tischer T, Predin M, Dendooven T, McLaughlin SH,
904 Barford D (2022) Structure of the human inner kinetochore bound to a centromeric CENP-A
905 nucleosome. *Science* 376: 844-852
906 Yatskevich S, Yang J, Bellini D, Zhang Z, Barford D (2024) Structure of the human outer kinetochore KMN
907 network complex. *Nat Struct Mol Biol* 31: 874-883
908 Zahm JA, Harrison SC (2024) A communication hub for phosphoregulation of kinetochore-microtubule
909 attachment. *Curr Biol* 34: 2308-2318 e2306

910

911

912 ## Main Figure Legends

913 **Figure 1: Mutation of the Kre28 helical bundle renders yeast cells inviable in the**
914 **presence of benomyl**

915 A: AlphaFold2 structure prediction of the Spc105$^{490-917}$/Kre28 heterodimer. The unstructured
916 N-terminal half of Spc105 was omitted form the structure prediction. Functionally relevant
917 regions of the proteins such as Zwint or RWD domains are labelled in distinct colors.

918 B: Secondary structure prediction of *S. cerevisiae* Zwint (top), *H. sapiens* Zwint (bottom) and
919 multiple sequence alignment of the so called Zwint helix of related eukaryotic proteins (middle).
920 Functional regions of Kre28 required for Spc105 (Roy *et al*, 2022), Mtw1c binding
921 (Ghodgaonkar-Steger *et al*, 2020), the C-terminal RWD domain (Tromer *et al*, 2019) and the
922 newly identified Zwint helix are marked.

923 C: Representative images of dissection plates of diploid heterozygous Kre28/Kre28-6xFlag
924 yeast strains with different 6xFlag-tagged alleles (WT, *ΔZwint*, *ΔRWD* or *ΔZwint ΔRWD*).
925 Strains were sporulated and dissected and the plates were incubated at 30 °C for three days.
926 Spores were subsequently analyzed regarding their genotype. While haploid strains with single
927 deletion of either the Zwint helix or the RWD domain are viable, simultaneous deletion of both
928 domains does not support viability of haploid yeasts.

929 D: Western blot analysis to compare protein expression levels of Kre28^{WT}, *kre28$^{\Delta Zwint}$* and
930 *kre28$^{\Delta RWD}$* in haploid yeast strains. Pgk1 was used as loading control.

931 E: Serial dilution assay of haploid yeast strains with different Kre28 alleles. Strains with the
932 indicated genotypes were serially diluted, spotted on YEPD or YEPD + benomyl plates and
933 incubated at the indicated temperatures. A *mad1*Δ strain was used as control for benomyl
934 hypersensitivity.

935

936 **Figure 2: The Kre28 helical bundle mutant displays defects in tension-dependent error-**
937 **correction**

938 A: Analysis of cell cycle progression. Haploid yeast strains with either Kre28^{WT}, *kre28$^{\Delta Zwint}$* or
939 *mad1*Δ were first arrested in G1 using α factor and then released into medium containing
940 nocodazole to depolymerize microtubules and test for functionality of the spindle assembly
941 checkpoint. Samples for western blot analysis were collected every 30 minutes and were
942 analyzed for Pds1 levels as readout for mitotic progression. A *mad1*Δ strain was used as
943 positive control for spindle assembly checkpoint deficiency.

944 B: Serial dilution assay of haploid yeast strains with Kre28^{WT} or *kre28$^{\Delta Zwint}$* in a *MAD1* or *mad1*Δ
945 strain background. Strains with the indicated genotypes were serially diluted, spotted on YEPD
946 or YEPD + benomyl plates and incubated at the indicated temperatures.

947 C: Analysis of cell cycle progression after release from a nocodazole arrest. Kre28^{WT} or

948 *kre28$^{\Delta Zwint}$* cells were arrested in mitosis using nocodazole and released into medium with
949 alpha factor to arrest cells in the next G1 phase. Samples were collected every 15 minutes
950 and Pds1 levels as marker for mitotic progression were analyzed by western blot. Pgk1 served
951 as loading control.
952 D and E: Analysis of segregation of fluorescently labelled chromosome XII by live cell
953 microscopy. Kre28^{WT} and *kre28$^{\Delta Zwint}$* cells with fluorescently labelled chromosome XII (CEN12-
954 GFP) and spindle pole bodies (Spc42-mCherry) were released from a nocodazole arrest and
955 segregation of chromosome XII during the next anaphase was followed. Representative
956 images of segregation and missegregation are shown in D, a quantification of the
957 missegregation rate is shown in E. Data is derived from three independent experiments
958 analyzing n > 100 cells per condition. The dots represent the data of each individual
959 experiment. Error bars indicate standard deviation. p value was calculated by an unpaired t-
960 test. **** = p < 0.0001. Exact p-value for E: p < 0.0001.
961 F: Representative images of dissection plates of diploid heterozygous Kre28/Kre28-6xFlag
962 Ipl1/*ipl1-1* strains. Strains were sporulated and dissected and the plates were incubated at
963 30 °C for three days. Afterwards, the spores were analyzed regarding their genotype. Haploid
964 strains with both *kre28$^{\Delta Zwint}$* and *ipl1-1* are viable but display severe growth retardation.
965 G: Summary of genetic interactions between the *kre28$^{\Delta Zwint}$* allele and mutant alleles of outer
966 kinetochore subunits (*ndc80-1*, *duo1$^{\Delta SxIP}$*, *dam1-1* and *dam1-9*), the Ndc80c recruiter Cnn1
967 (*cnn1Δ*), CPC subunits (*ipl1-1*, *sli15-3*), CPC recruiters (*sgo1Δ*, *ctf19$^{\Delta C\text{-}RWD}$*) or a spindle
968 assembly checkpoint component (*mad1Δ*).
969

970 **Figure 3: The Kre28$^{\Delta Zwint}$ mutant reduces the level of Spc105/Kre28 at kinetochore**
971 **clusters *in vivo***
972 A: Live cell imaging of yeast cells with GFP-tagged Mtw1- and Nuf2 subunits. Representative
973 images of metaphase and anaphase cells are shown on the left, quantification of fluorescence
974 signal intensities on the right. Kinetochore recruitment of Mtw1-GFP (Mtw1 complex), Nuf2-
975 GFP (Ndc80 complex) was analyzed in Kre28^{WT} and *kre28$^{\Delta Zwint}$* strain backgrounds. The C-
976 terminus of Spc42 was fused to RFP to label the position of the mitotic spindle. The mean of
977 metaphase signal intensities in the wildtype strain was defined as 1 and all other data was
978 normalized to this value. Means +/- standard deviation are plotted. p-values were calculated
979 with a Kruskal-Wallis test and are displayed as follows: n.s. non-significant = p-value > 0.05;
980 **** = p < 0.0001. Exact p-values from (A): n.s. > 0.9999 in all cases, except Mtw-GFP
981 anaphase wt versus Δzwint p = 0.5820; **** p < 0.0001 in all cases. n > 100 kinetochore
982 clusters were analyzed for each condition. Representative data from at least two independent
983 experiments is shown.

984 B: Live cell imaging of yeast cells with GFP-tagged Spc105 and GFP-Kre28. Representative
985 images of metaphase and anaphase cells are shown on the left, quantification of fluorescence
986 signal intensities on the right. Kinetochore recruitment of Spc105 was analyzed in Kre28^{WT} and
987 *kre28$^{\Delta Zwint}$* strain backgrounds. GFP-Kre28 was analyzed as wildtype and Δzwint mutant. The
988 C-terminus of Spc42 was fused to RFP to label the position of the mitotic spindle. The mean
989 of metaphase signal intensities in the wildtype strain was defined as 1 and all other data was
990 normalized to this value. Means +/- standard deviation are plotted. p values were calculated
991 with a Kruskal-Wallis test and displayed as follows: n.s. non-significant = p-value > 0.05; **** =
992 p < 0.0001; *** = p < 0.001; Exact p-values from (B): **** p < 0.0001 in all cases; *** = p =
993 0.0003. n > 100 kinetochore clusters were analyzed for each condition. Representative data
994 from at least two independent experiments is shown.
995
996 **Figure 4: Artificial recruitment of Sli15 to Mtw1 suppresses the *kre28$^{\Delta Zwint}$* mutant**
997 **phenotype**
998 A: Illustration of artificial recruitment of Ipl1 to KMN by fusion of a C-terminal fragment of Sli15
999 to the C-terminus of Mtw1 and schematic of the architecture of two different Mtw1-Sli15 fusion
1000 proteins. Two C-terminal fragments of Sli15 were fused to the C-terminus of Mtw1, separated
1001 by a 6xHA tag. Ipl1 is recruited to the fusion proteins by binding to the IN box of Sli15. The red
1002 asterisks mark the position of W646G and F680A amino acid substitutions which prevent
1003 binding of Ipl1 to Sli15. The genes encoding the fusion constructs were integrated at the *LYS2*
1004 locus and under control of the Mtw1 promotor.
1005 B: Western blot analysis of Mtw1 fusion proteins and Kre28 mutants. Extracts of indicated
1006 strains were blotted for the presence of fusion proteins (anti-HA), Kre28 wildtype or mutant
1007 (anti-Flag).
1008 C: Serial dilution assay with haploid yeast strains with Kre28^{WT} or *kre28$^{\Delta Zwint}$* expressing
1009 different Mtw1-Sli15 fusion proteins. Serial dilutions of yeast strains with the indicated
1010 genotypes were spotted on YEPD and YEPD + benomyl plates and incubated at the indicated
1011 temperatures.
1012 D: Scoring of chromosome segregation in Kre28^{WT} or *kre28$^{\Delta Zwint}$* with fluorescently labelled
1013 chromosome XII (CEN12-GFP) and spindle pole bodies (Spc42-mCherry) expressing different
1014 Mtw1-Sli15 fusion proteins. Cells were released from a nocodazole arrest and segregation of
1015 chromosome XII in the first anaphase after release was analyzed. Missegregation rates in the
1016 different strains are displayed with data from three independent experiments. Mean values +/-
1017 standard deviation are plotted. The dots represent the data from three individual experiments.
1018 n > 110 cells were analyzed for each condition in each experiment. p values were calculated
1019 with an unpaired t-test.
1020

1021 **Figure 5: Ipl1/Sli15 binds to KMN via the Spc105/Kre28 subcomplex *in vitro***
1022 A: Single-step isolation of a recombinant budding yeast KMN network from Sf9 insect cells.
1023 Left side shows Coomassie-stained SDS-PAGE of anti-Flag purification of Spc105-Flag. Right
1024 panel shows consecutive fractions from size exclusion chromatography on a Superose 6
1025 column.
1026 B: Gallery of electron micrographs showing recombinant KMN network visualized by Pt/C
1027 rotary shadowing EM. Distinct configurations are shown in which the end of the Ndc80 complex
1028 shows one or more appendages. Scale bar: 50 nm.
1029 C: Pull down assays to test for binding of Ipl1/Sli15 to KMN. KMN containing either $Kre28^{WT}$ or
1030 $Kre28^{\Delta Zwint}$ was purified from Sf9 insect cells and immobilized on M2 anti-Flag beads.
1031 Recombinant Ipl1/Sli15 was added to test for its binding to KMN. Proteins were eluted from
1032 beads by addition of 3xFlag peptide. Input and pull down samples were analyzed by SDS-
1033 PAGE and Coomassie staining or western blot to detect 6xHis-tagged Sli15.
1034 D: Pull down assay to test for binding of Ipl1/Sli15 to Spc105/Kre28 or Mtw1c/Ndc80c. Either
1035 Spc105/Kre28 or Mtw1c in combination with Ndc80c were purified from Sf9 insect cells and
1036 immobilized on M2 anti-Flag beads. Recombinant Ipl1/Sli15 was added to test for its binding
1037 to the immobilized proteins. Proteins bound to the beads were finally eluted with 3xFlag peptide
1038 and input and pull down samples were analyzed by SDS-PAGE followed by Coomassie
1039 staining or western blot to detect 6xHis-tagged Sli15. Asterisk denotes potential proteolysis
1040 product of full-length Spc105.
1041 E: Pull down assay to analyze the impact of Ipl1/Sli15 phosphorylation on binding to
1042 Spc105/Kre28. Spc105/Kre28 was purified from Sf9 insect cells and immobilized on M2 anti-
1043 Flag beads. Prior to addition to the loaded beads, recombinant Ipl1/Sli15 was *in vitro*
1044 autophosphorylated (+ATP), dephosphorylated by λ phosphatase or left untreated. After
1045 incubation with the immobilized Spc105/Kre28, bound proteins were eluted from the beads
1046 using 3xFlag peptide and input and pull down samples were analyzed by SDS-PAGE and
1047 Coomassie staining or western blot to detect 6xHis-Sli15. The mobility of Ipl1 and Sli15 during
1048 SDS-PAGE depends on their phosphorylation status. LC and HC mark the light and heavy
1049 chains of the M2 anti-Flag antibody. Asterisk denotes potential proteolysis product of full-length
1050 Spc105.
1051 F: *In vivo* proximity-biotinylation experiment using Spc105-TurboID and different Flag-tagged
1052 potential interactors. Yeast lysates were prepared from the indicated strains and subjected to
1053 a Streptavidin affinity purification to isolate biotinylated proteins. Note that Kre28 and Sli15 are
1054 only detected in pull downs from strains that also express Spc105-TurboID. The major
1055 endogenously biotinylated proteins Acc1, Pyc1/2 or Arc1 enriched in in the Streptavidin pull
1056 down are indicated.
1057

1058 **Figure 6: Chemical cross-linking mass spectrometry analysis of the KMN-Ipl1/Sli15**
1059 **assembly**
1060 A: Schematic illustration of Sli15 and Ipl1. Sli15 associates with its N-terminal CEN box to
1061 Bir1/Survivin and Nbl1/Borealin. The C-terminal IN box binds to the globular kinase domain of
1062 Ipl1.
1063 B: Network diagram of inter- and intramolecular Lys-Lys crosslinks of a KMN-Ipl1/Sli15
1064 assembly. Recombinant KMN and Ipl1/Sli15 were mixed at equimolar amounts and incubated
1065 in the presence of BS3. Functional domains of Ipl1 and Sli15 are indicated in the legend.
1066 Interlinks originating from Sli15 to KMN subunits are highlighted. Segments rich in crosslinks
1067 between Sli15 and Spc105 are boxed.
1068
1069 **Figure 7: Binding of a Sli15 segment to the Spc105/Kre28 helical bundle is critical for**
1070 **chromosome segregation in cells**
1071 A: Alphafold2 structure prediction of the Spc105/Kre28 helical bundle domain (dark red/dark
1072 blue) bound to Sli15 segment 215-255 (orange). Scheme on top indicates the position of the
1073 peptide in the Sli15 domain organization.
1074 B. Details of the predicted Sli15 binding interface. Surface of Spc105/Kre28 is indicated as
1075 electrostatic potential (red: negatively charged, blue positively charged, white: neutral).
1076 Predicted key Sli15 residues and their side chains are highlighted.
1077 C: Multiple sequence alignment of the Sli15 segment from different yeast species. MSA was
1078 generated in Jalview and colored based on conservation. Position of residues mutated in the
1079 *sli15*^{4E} mutant is indicated. Abbreviations as follows: *S.*: *Saccharomyces*, *K.*: *Kluyveromyces,*
1080 *C.*: *Candida.* The proximal Sli15 residue K217 was found to crosslink to Spc105 (Figure 5).
1081 D: Pull down assay with recombinant Spc105/Kre28 and Ipl1/6xHis-Sli15 wildtype or Sli15^{4E}
1082 mutant. After incubation with the immobilized Spc105/Kre28, bound proteins were eluted from
1083 the beads using 3xFlag peptide and input and pull down samples were analyzed by SDS-
1084 PAGE and Coomassie staining or western blot to detect 6xHis-Sli15. 6xHis-Sli15 signals were
1085 quantified in the pull down and normalized to the wildtype.
1086 E: Representative images of dissection plates from diploid Sli15/Sli15-6xFlag strains, in which
1087 the Sli15-6xFlag allele encodes for either Sli15^{wt}, sli15^{4E}, sli15$^{\Delta N}$, or sli15$^{\Delta N,\ 4E}$. Circled spores
1088 indicate the recovered or inferred Sli15-6xFlag tagged variants.
1089 F: Left: representative micrographs of diploid cells in late anaphase. The cells are
1090 heterozygous for Mtw1/Mtw1-mCherry and Sli15/Sli15-mNeonGreen(mNG)-6xFlag. The
1091 integrated locus of Sli15 encodes for either Sli15^{wt}, sli15^{4E}, sli15$^{\Delta N}$, or sli15$^{\Delta N,\ 4E}$. Scale bar:
1092 2 µm. Right: line scan analysis of the intensity of Mtw1-mCherry and Sli15-mNeonGreen along
1093 the anaphase spindle in the cells depicted on the left. Only Sli15$^{\Delta N}$ shows sharp peaks for
1094 Sli15-mCherry that co-localize with the peaks for Mtw1-mCherry.

1095 G: Quantification of the fraction of anaphase spindles that show Sli15-mNeonGreen foci at
1096 spindle poles, overlapping with the Mtw1-mCherry foci, as represented in F. The points indicate
1097 the fraction in three replicates, the bar depicts the mean with standard deviation. Statistical
1098 analysis: unpaired t-test comparing between wildtype and 4E. n.s. non-significant $p > 0.05$, * =
1099 $p < 0.05$. Exact p-values for (G) n.s. $p = 0.6972$, * $p = 0.0219$.
1100

1101 **Figure 8: A model for Ipl1/Sli15 docking to the outer kinetochore**
1102 A: Organization of centromere-binding modules and outer kinetochore docking sites in the
1103 Ipl1/Sli15 complex.
1104 B: Model for how conformation-sensitive outer kinetochore docking could contribute to tension-
1105 dependent error correction. To improve clarity the disordered N-terminus of Spc105 has been
1106 omitted. A crucial interface between a Sli15 segment and the Spc105/Kre28 helix bundle is
1107 highlighted.

1108

1109

1110 ## Expanded Figure Legends

1111 **Figure EV1 – refers to Figure 1: Detailed mutagenesis analysis of the Zwint helix**
1112 A: Multiple sequence alignment of Kre28 sequences from different yeast species. Conserved
1113 residues are colored according to the Clustal color scheme. Positions of smaller Zwint helix
1114 deletions and alanine substitutions of conserved residues are marked.
1115 B: Western blot analysis of different Kre28/Zwint deletion or point mutants. Extracts of log
1116 phase yeast cells were analyzed, Pgk1 blot serves as a loading control.
1117 C and D: Serial dilution assays of haploid yeast strains with different Kre28 Zwint helix
1118 deletions or point mutations of conserved residues. Strains with the indicated genotypes were
1119 serially diluted and spotted on YEPD or YEPD + benomyl plates and incubated at the indicated
1120 temperatures.
1121

1122 **Figure EV2 - refers to Figure 3: Western blot analysis of GFP-tagged KMN subunits and**
1123 **live cell microscopy of Sgo1-GFP**
1124 A: Western blot analysis to compare the expression of different GFP-tagged KMN subunits. in
1125 Kre28 wildtype and mutant cells. Pgk1 served as loading control.
1126 B: Western blot analysis of expression level of N-terminal GFP-tagged Kre28 in wildtype and
1127 mutant form.
1128 C: Western blot analysis of C-terminal GFP-tagged Kre28 in wildtype and mutant form.
1129 D: Quantification of Kre28-GFP fluorescence signals at metaphase and anaphase

1130 kinetochores. Strains with either Kre28^{WT}-GFP or *kre28$^{\Delta Zwint}$*-GFP were analyzed by live cell
1131 microscopy. The C-terminus of Spc42 was fused to RFP to label the position of the mitotic
1132 spindle. The mean of metaphase signal intensities in the wildtype strain was defined as 1 and
1133 all other data was normalized to this value. Means +/- standard deviation are plotted. p values
1134 were calculated with a Kruskal-Wallis test, and displayed as follows: **** = $p < 0.0001$. Exact
1135 p-values for E: in all cases **** < 0.0001. n > 100 kinetochore clusters were analyzed for each
1136 condition. Representative data from two independent experiments is shown.
1137 E: Live cell microscopy for analysis of Sgo1-GFP kinetochore localization in a Kre28^{WT} or
1138 *kre28$^{\Delta Zwint}$* strain background. Representative images of a metaphase and an anaphase cell
1139 are shown on the left and quantification of Sgo1-GFP signals in cells with short mitotic spindles
1140 is shown on the right. Data was normalized to the mean value measured for the Kre28^{WT} strain.
1141 Mean values +/- standard deviation are plotted. A Mann-Whitney test was used to test for
1142 statistical significance.
1143

1144 **Figure EV3 – refers to Figure 5: Pull -down experiment and *in vitro* kinase reaction with**
1145 **Ipl1/Sli15 and KMN**
1146 A: Pull down assays to analyze binding of Ipl1/Sli15 to KMN. KMN with either Kre28^{WT} or
1147 Kre28$^{\Delta Zwint}$ was purified from Sf9 cells and immobilized on M2 anti-Flag beads. Loaded beads
1148 were incubated with buffer or recombinant Ipl1/Sli15, afterwards proteins bound to the beads
1149 were eluted with 3xFlag peptide. Input and pull down samples were analyzed by SDS-PAGE
1150 and Coomassie staining or western blot to detect 6xHis-tagged Sli15.
1151 B: *In vitro* kinase reaction with Ipl1/Sli15 or Ipl1/Sli15 in presence of recombinant KMN
1152 analyzed over time. Coomassie stained gel at the top, corresponding autoradiograph at the
1153 bottom. For control a KMN only sample taken 30 min after incubation with radioactive ATP is
1154 shown in the first lane. C: Quantification phosphorylated Ipl1 signal over time alone (blue curve)
1155 or in presence of KMN (green curve).
1156

1157 **Figure EV4 – refers to Figure 7**

1158 A. PAE plot of the top-ranked model of the Spc105 (449-642)-Kre28 (1-208)- Sli15 (215-255)
1159 complex. Fragment boundaries are indicated by black lines, blue are favorable scores, red are
1160 unfavorable.
1161 B. Position of the Kre28 Zwint helix (light blue) in the top ranked model. Note that only a part
1162 of the Zwint helix is involved in the binding interface with Sli15, while the majority of the helix
1163 is on the opposite side of the Spc105/Kre28 bundle.
1164 C. Top row: Superposition of the ten top ranked models of the Sli15 peptide on Spc105/Kre28.
1165 pLDDT scores for the Sli15 peptides are indicated with blue and green showing favorable, and

1166 red unfavorable scores. The Spc105/Kre28 surface is colored by electrostatic potential.
1167 Bottom: Details of the top ranked model, with key side chains of the Sli15 peptide indicated as
1168 sticks. Coloring by pLDDT scores as above.

1169

1170 **Figure EV5 – refers to Figure 7**

1171 A. Serial dilution assay testing full-length Sli15 wildtype and -4E rescue constructs in a *sli15-*
1172 *aid* system. Three clones for wildtype and mutant are tested. Background indicates a strain
1173 lacking *sli15-aid*, no rescue indicates a *sli15-aid* strain without a Sli15 rescue construct.

1174 B. Serial dilution assay testing Sli15-ΔN wildtype and -4E rescue constructs in a *sli15-aid*
1175 system. Three clones for each version are tested. Background indicates a strain lacking sli15-
1176 aid, no rescue indicates a sli15-aid strain without a Sli15 rescue construct.

1177 C. Western Blot analysis of Sli15-Flag rescue constructs tested in A and B. Asterisk denotes
1178 unspecific band.

1179 D. Serial dilution assay testing the indicated Sli15 rescue constructs in a *sli15-aid* system.
1180 Three clones for each version (Sli15 R231E R232E, or Sli15 K242E) are tested.

1181 E. Left side: Details of the predicted binding site surrounding Sli15 K242 (orange) with
1182 interacting residues in Kre28 (dark blue) or Spc105 (dark red) highlighted. Right side: Details
1183 of the predicted binding site surrounding Sli15 residues R231 and R232.

1184 F. Serial dilution assay testing the effects of Spc105 mutations predicted to affect the Sli15
1185 binding site. Spc105 rescue constructs are tested in an Spc105-FRB anchor-away system in
1186 which upon rapamycin addition the endogenous Spc105 protein is removed from the nucleus.
1187 Three clones for wildtype rescue constructs, and two clones of each mutant are tested.

1188

1189

1190

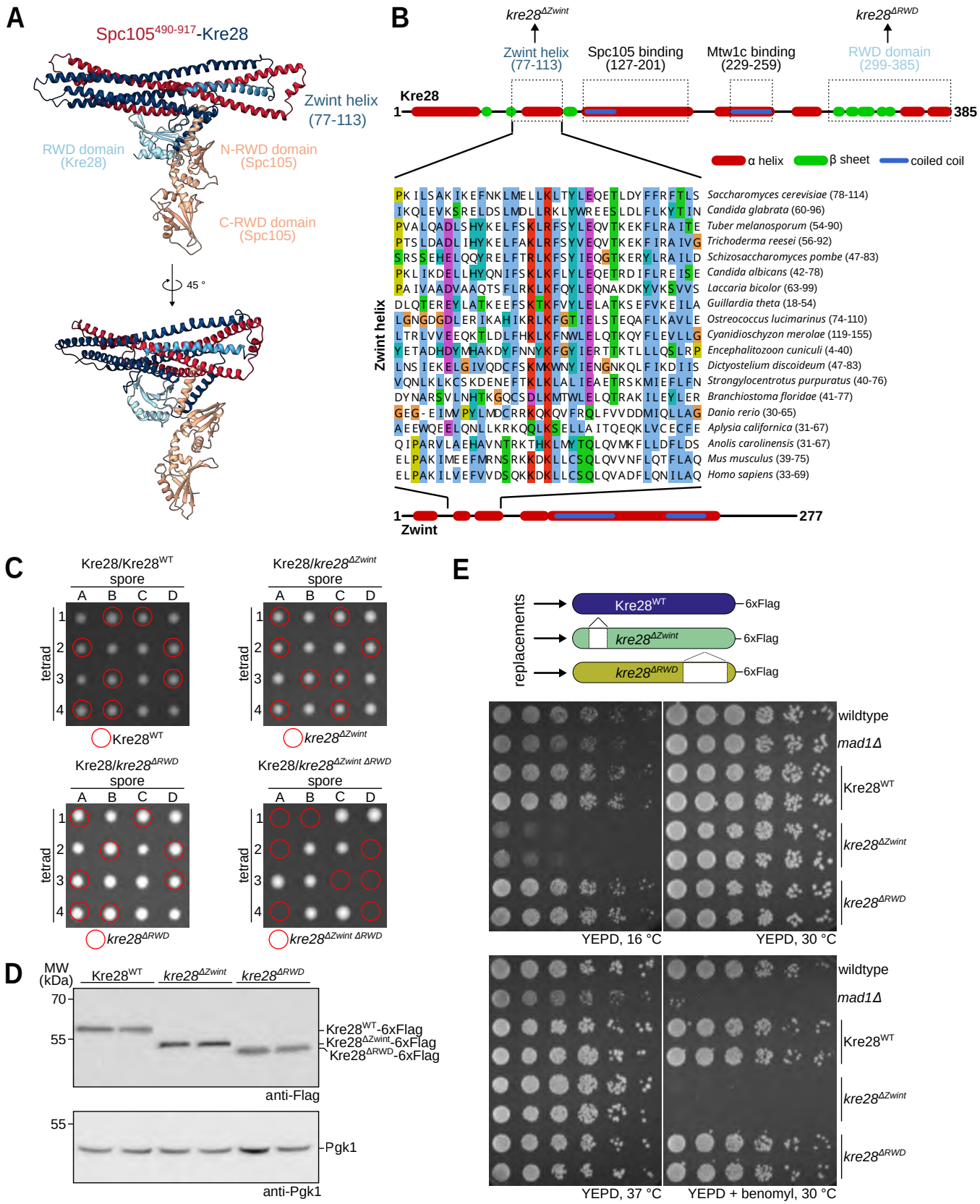
A
Spc105490-917-Kre28
Zwint helix (77-113)
RWD domain (Kre28)
N-RWD domain (Spc105)
C-RWD domain (Spc105)
45 °
B
kre28ΔZwint
kre28ΔRWD
Zwint helix (77-113)
Spc105 binding (127-201)
Mtw1c binding (229-259)
RWD domain (299-385)
Kre28
1
385
α helix
β sheet
coiled coil
Zwint helix
Saccharomyces cerevisiae (78-114)
Candida glabrata (60-96)
Tuber melanosporum (54-90)
Trichoderma reesei (56-92)
Schizosaccharomyces pombe (47-83)
Candida albicans (42-78)
Laccaria bicolor (63-99)
Guillardia theta (18-54)
Ostreococcus lucimarinus (74-110)
Cyanidioschyzon merolae (119-155)
Encephalitozoon cuniculi (4-40)
Dictyostelium discoideum (47-83)
Strongylocentrotus purpuratus (40-76)
Branchiostoma floridae (41-77)
Danio rerio (30-65)
Aplysia californica (31-67)
Anolis carolinensis (31-67)
Mus musculus (39-75)
Homo sapiens (33-69)
1
Zwint
277
C
Kre28/Kre28WT
Kre28/kre28ΔZwint
Kre28/kre28ΔRWD
Kre28/kre28ΔZwint ΔRWD
spore
A B C D
tetrad
1 2 3 4
Kre28WT
kre28ΔZwint
kre28ΔRWD
kre28ΔZwint ΔRWD
D
MW (kDa)
Kre28WT
kre28ΔZwint
kre28ΔRWD
70
55
Kre28WT-6xFlag
Kre28ΔZwint-6xFlag
Kre28ΔRWD-6xFlag
anti-Flag
55
Pgk1
anti-Pgk1
E
replacements
Kre28WT
kre28ΔZwint
kre28ΔRWD
6xFlag
wildtype
mad1Δ
Kre28WT
kre28ΔZwint
kre28ΔRWD
YEPD, 16 °C
YEPD, 30 °C
YEPD, 37 °C
YEPD + benomyl, 30 °C

Figure EV1 - refers to Figure 1

Dudziak et al., 2025

A

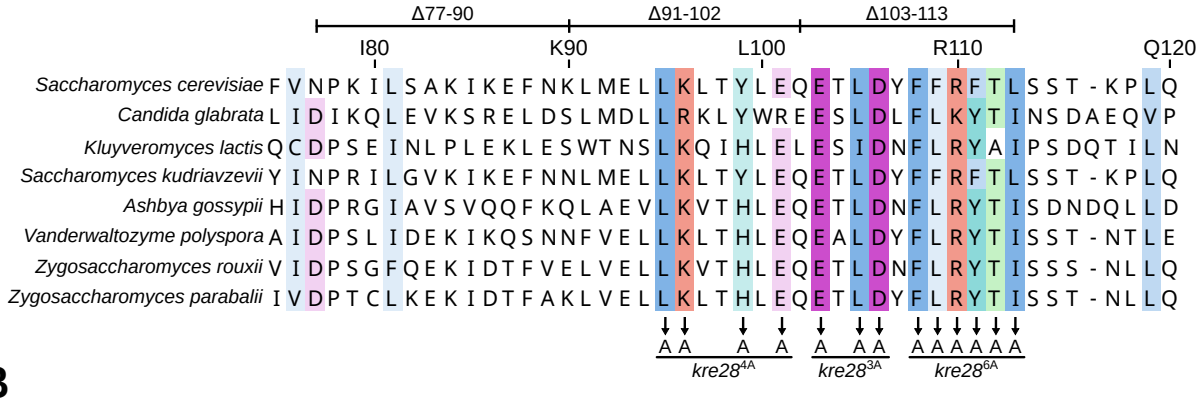

B

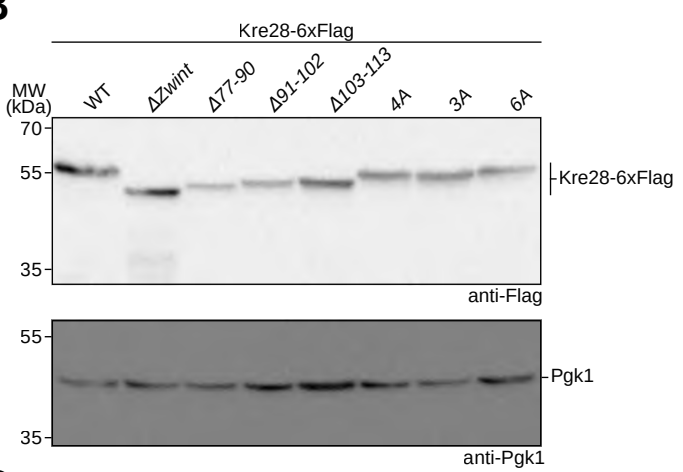

C

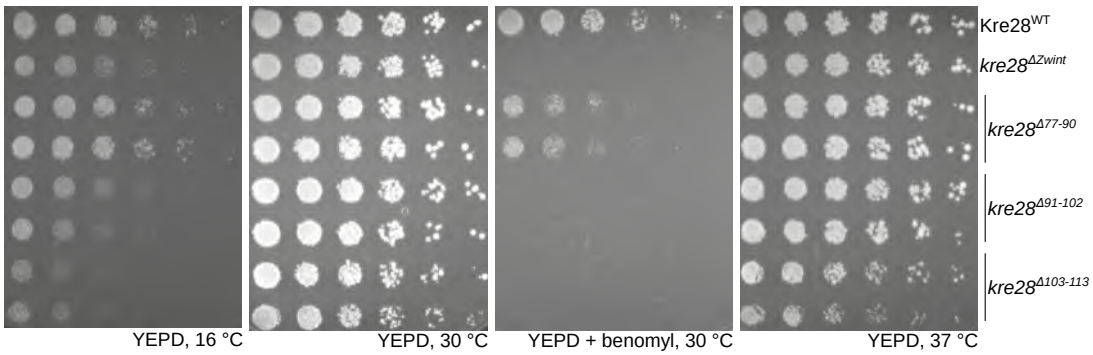

D

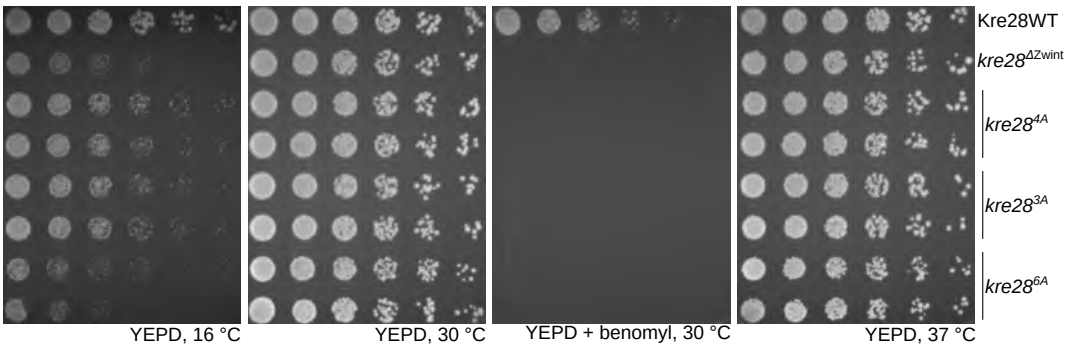

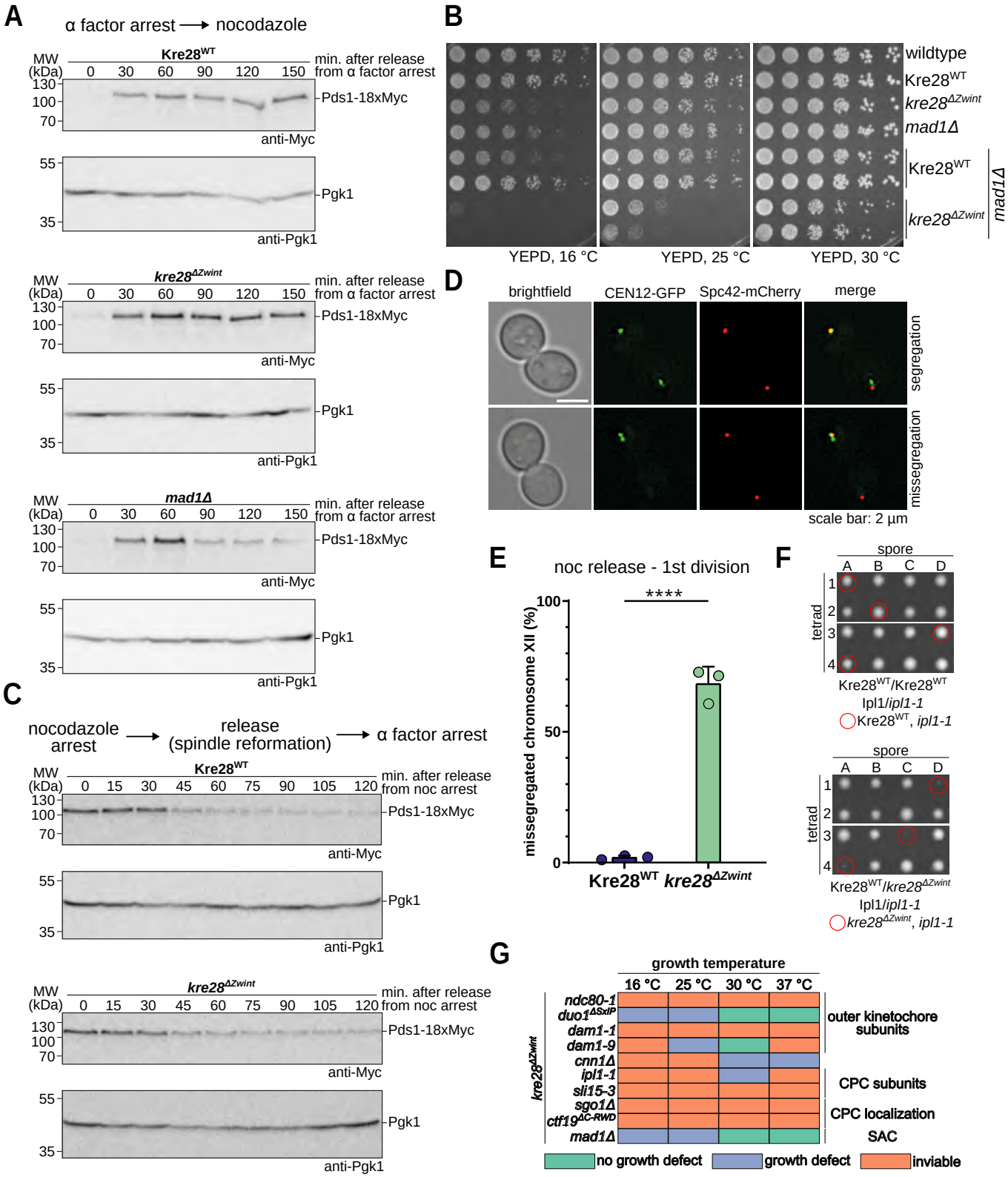
A
α factor arrest → nocodazole
Kre28WT
MW (kDa)
0 30 60 90 120 150
min. after release from α factor arrest
130
100
70
Pds1-18xMyc
anti-Myc
55
35
Pgk1
anti-Pgk1
kre28ΔZwint
mad1Δ
B
wildtype
Kre28WT
kre28ΔZwint
mad1Δ
YEPD, 16 °C
YEPD, 25 °C
YEPD, 30 °C
C
nocodazole arrest → release (spindle reformation) → α factor arrest
0 15 30 45 60 75 90 105 120
min. after release from noc arrest
D
brightfield
CEN12-GFP
Spc42-mCherry
merge
segregation
missegregation
scale bar: 2 µm
E
noc release - 1st division
****
missegregated chromosome XII (%)
100
50
0
Kre28WT
kre28ΔZwint
F
spore
A B C D
tetrad
1
2
3
4
Kre28WT/Kre28WT
Ipl1/ipl1-1
Kre28WT, ipl1-1
Kre28WT/kre28ΔZwint
kre28ΔZwint, ipl1-1
G
growth temperature
16 °C 25 °C 30 °C 37 °C
ndc80-1
duo1ΔSxIP
dam1-1
dam1-9
cnn1Δ
ipl1-1
sli15-3
sgo1Δ
ctf19ΔC-RWD
mad1Δ
outer kinetochore subunits
CPC subunits
CPC localization
SAC
no growth defect
growth defect
inviable

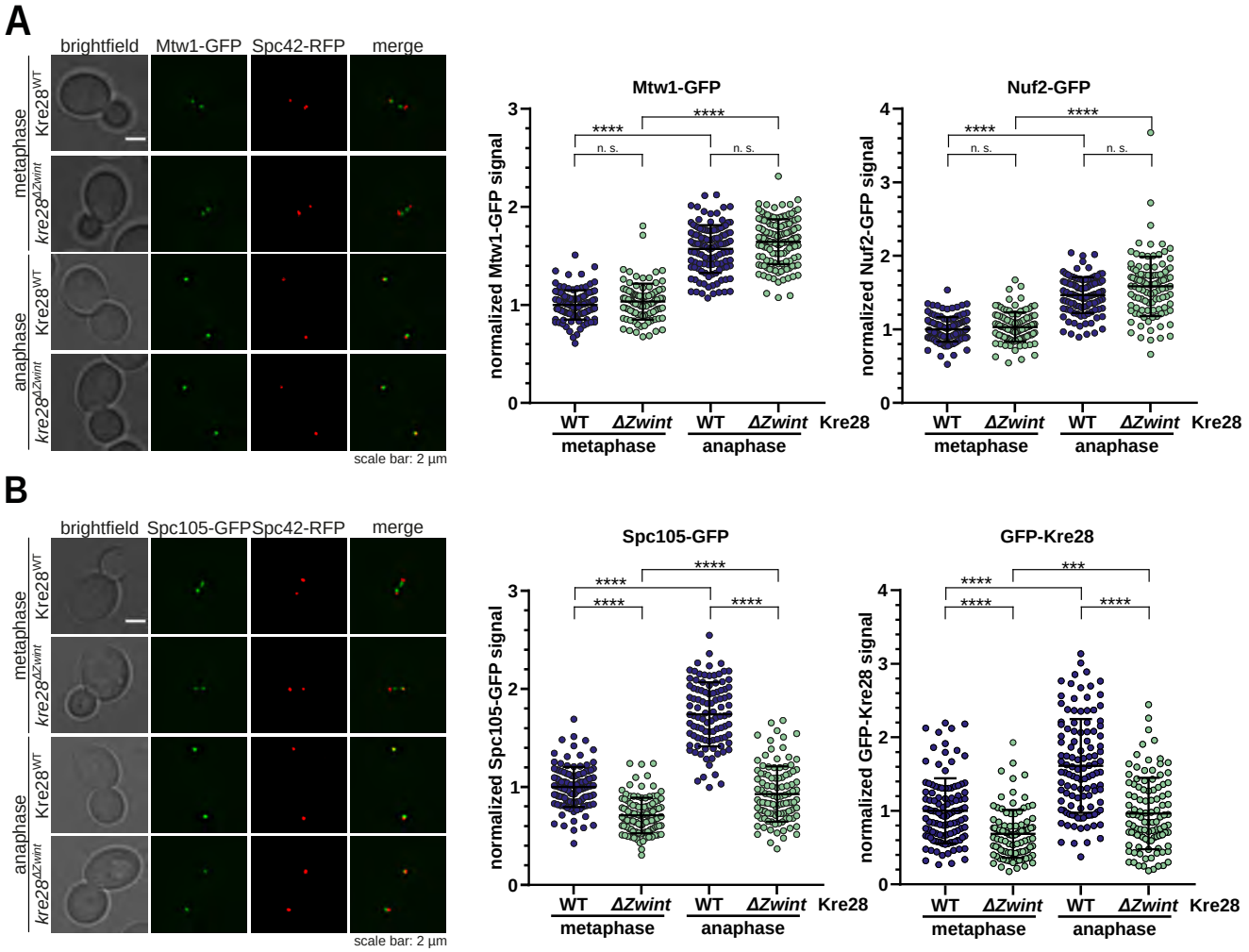
A
brightfield
Mtw1-GFP
Spc42-RFP
merge
metaphase
anaphase
Kre28WT
kre28ΔZwint
scale bar: 2 µm
Mtw1-GFP
normalized Mtw1-GFP signal
Nuf2-GFP
normalized Nuf2-GFP signal
****
n. s.
WT
ΔZwint
Kre28
B
brightfield
Spc105-GFP
Spc42-RFP
merge
Spc105-GFP
normalized Spc105-GFP signal
GFP-Kre28
normalized GFP-Kre28 signal
***

Figure EV2 - referring to Figure 3

Dudziak et al., 2025

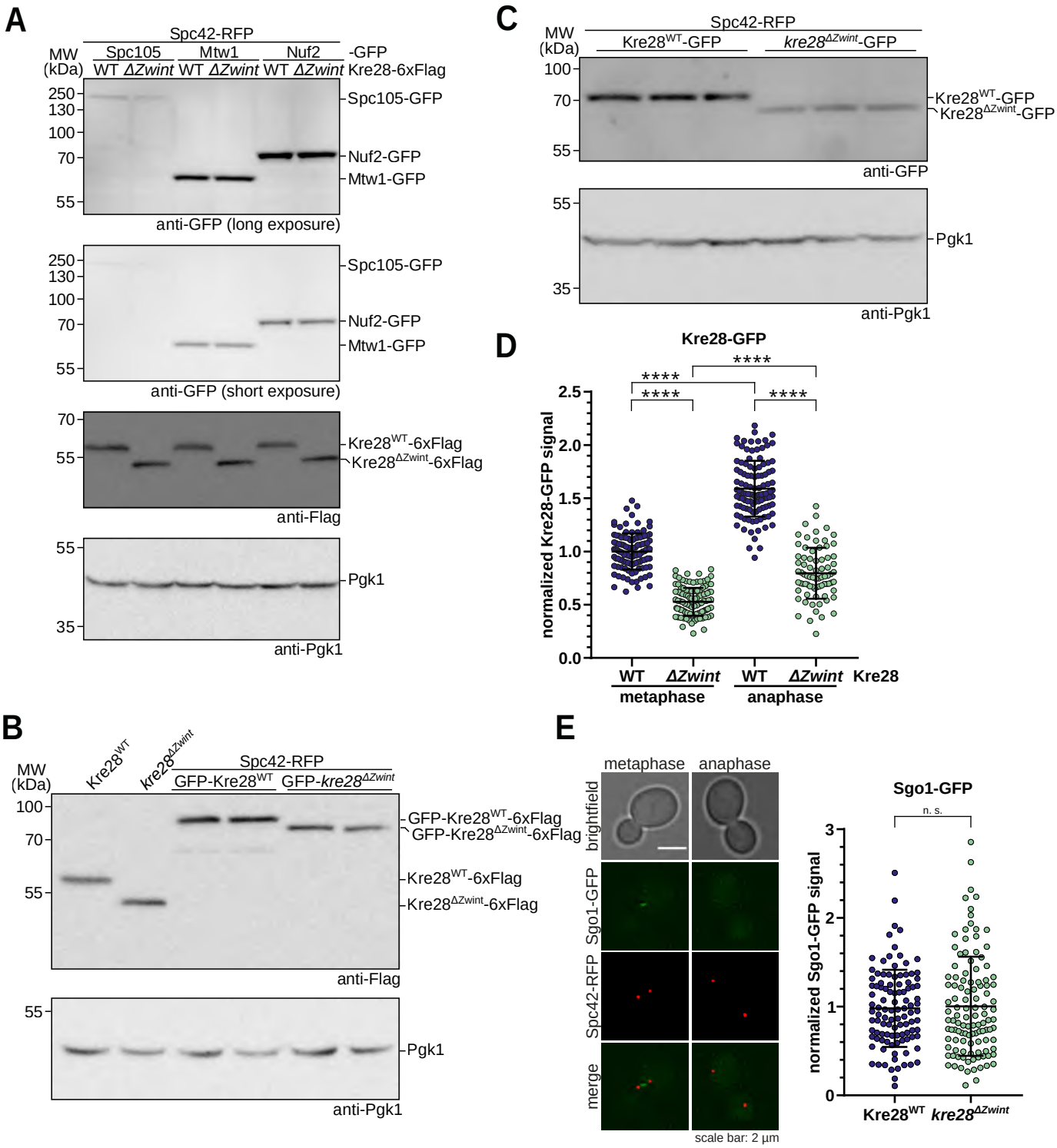

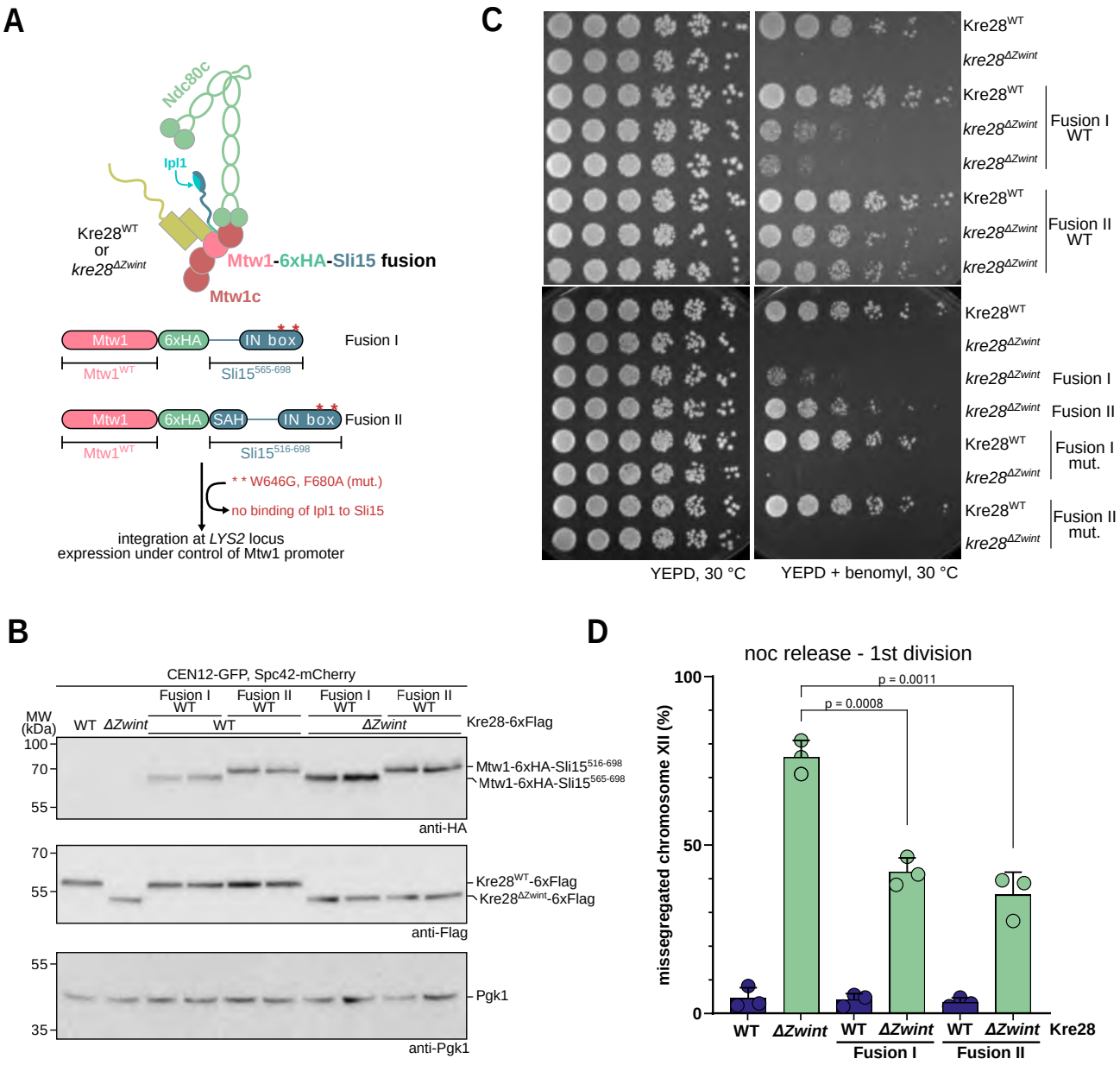
A
Ndc80c
Ipl1
Kre28WT or kre28ΔZwint
Mtw1-6xHA-Sli15 fusion
Mtw1c
Mtw1
6xHA
IN box
Fusion I
Mtw1WT
Sli15565-698
Mtw1
6xHA
SAH
IN box
Fusion II
Mtw1WT
Sli15516-698
* * W646G, F680A (mut.)
no binding of Ipl1 to Sli15
integration at LYS2 locus
expression under control of Mtw1 promoter
C
Kre28WT
kre28ΔZwint
Fusion I WT
Fusion II WT
Fusion I
Fusion II
Fusion I mut.
Fusion II mut.
YEPD, 30 °C
YEPD + benomyl, 30 °C
B
CEN12-GFP, Spc42-mCherry
MW (kDa)
WT
ΔZwint
Fusion I WT
Fusion II WT
Kre28-6xFlag
Mtw1-6xHA-Sli15516-698
Mtw1-6xHA-Sli15565-698
anti-HA
Kre28WT-6xFlag
Kre28ΔZwint-6xFlag
anti-Flag
Pgk1
anti-Pgk1
D
noc release - 1st division
missegregated chromosome XII (%)
p = 0.0011
p = 0.0008
WT
ΔZwint
Fusion I
Fusion II
Kre28

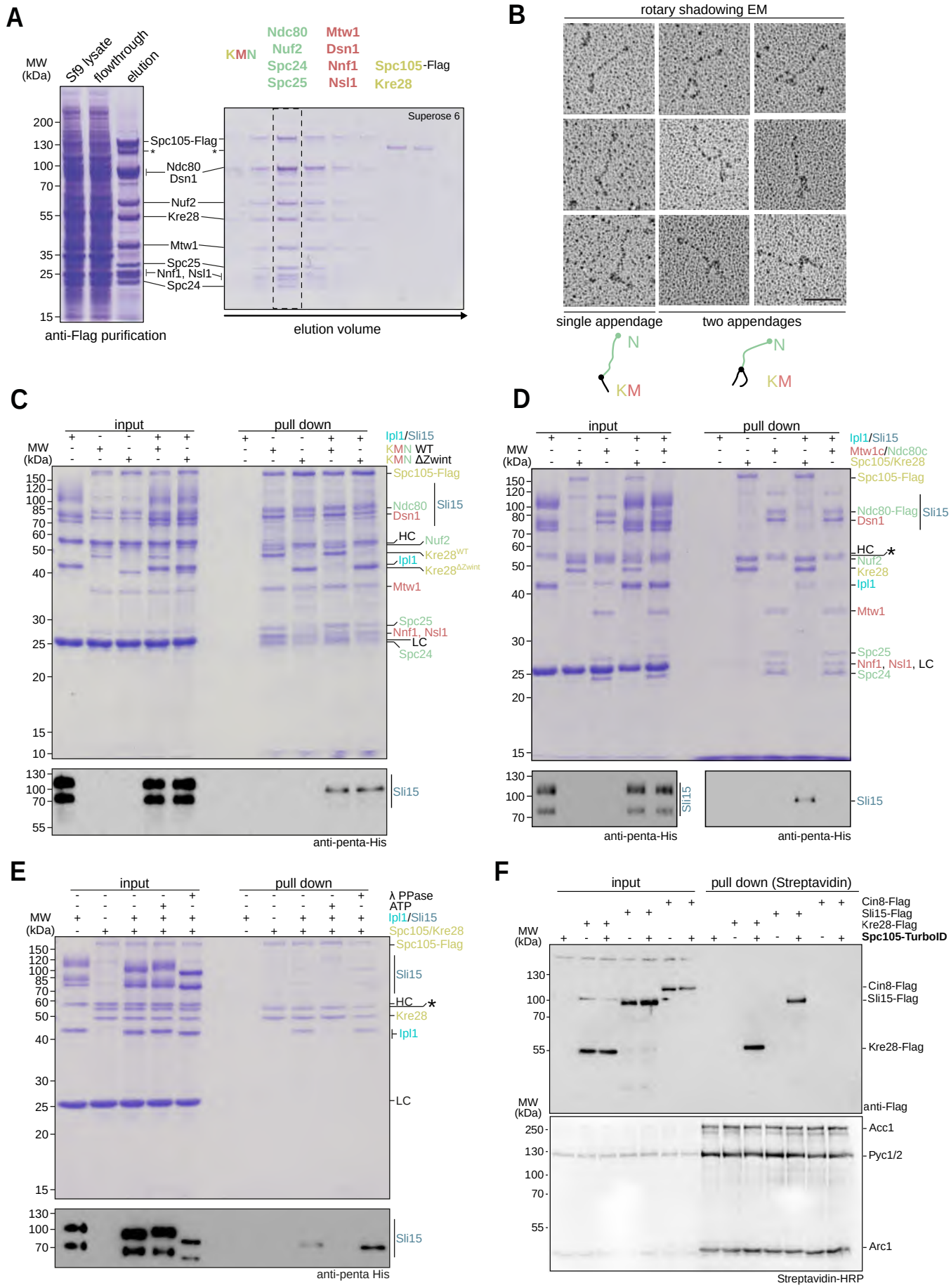
A
MW (kDa)
Sf9 lysate
flowthrough
elution
KMN
Ndc80
Nuf2
Spc24
Spc25
Mtw1
Dsn1
Nnf1
Nsl1
Spc105-Flag
Kre28
Superose 6
Spc105-Flag
Ndc80
Dsn1
Nuf2
Kre28
Mtw1
Spc25
Nnf1, Nsl1
Spc24
anti-Flag purification
elution volume
B
rotary shadowing EM
single appendage
two appendages
N
KM
C
input
pull down
Ipl1/Sli15
KMN WT
KMN ΔZwint
Spc105-Flag
Ndc80
Dsn1
Sli15
HC
Nuf2
Kre28WT
Ipl1
Kre28ΔZwint
Mtw1
Spc25
Nnf1, Nsl1
LC
Spc24
anti-penta-His
D
Mtw1c/Ndc80c
Spc105/Kre28
Ndc80-Flag
anti-penta-His
E
λ PPase
ATP
anti-penta His
F
input
pull down (Streptavidin)
Cin8-Flag
Sli15-Flag
Kre28-Flag
Spc105-TurboID
anti-Flag
Acc1
Pyc1/2
Arc1
Streptavidin-HRP

Figure EV3 - refers to Figure 5

Dudziak et al., 2025

A

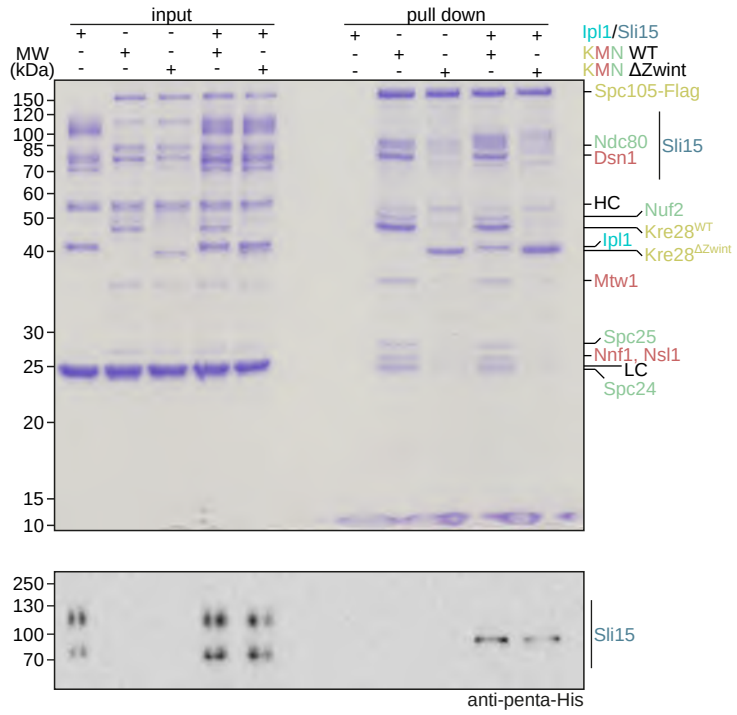

B

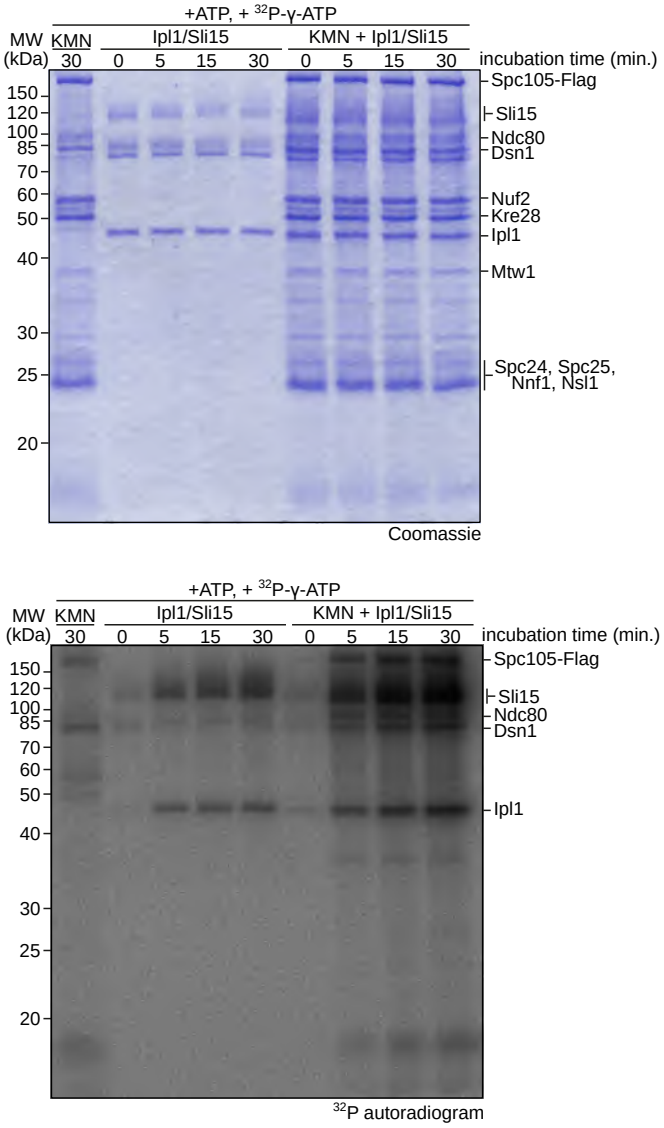

C

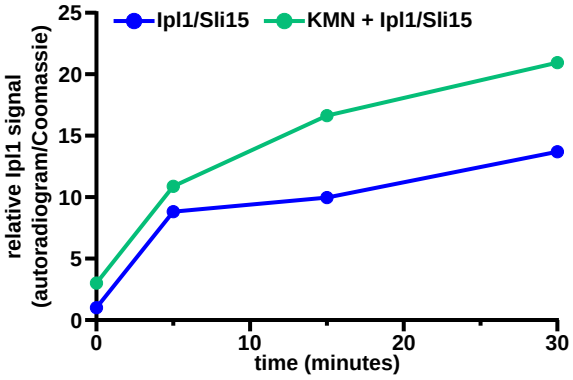

Figure 6 **Dudziak et al., 2025**

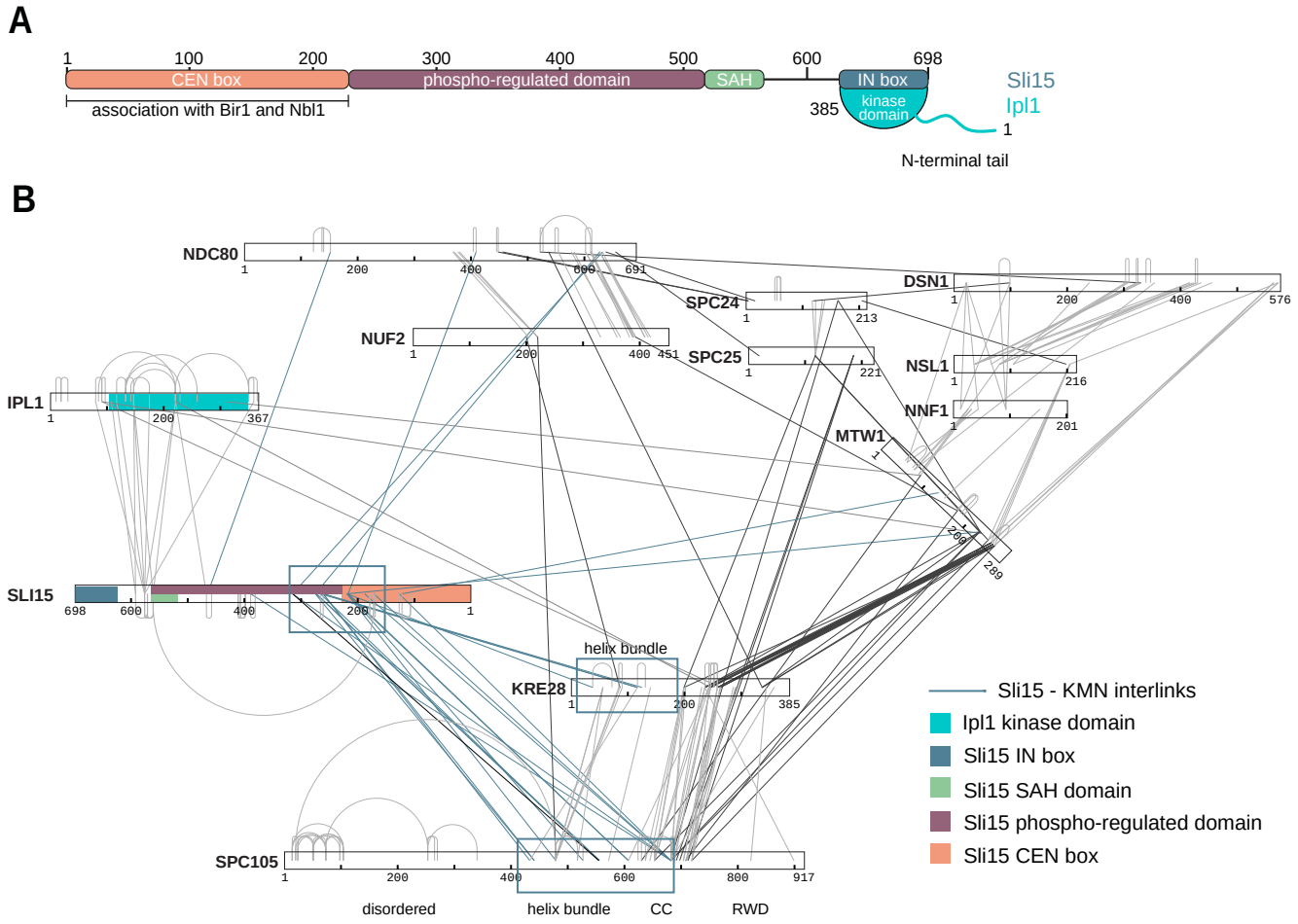

Figure 7

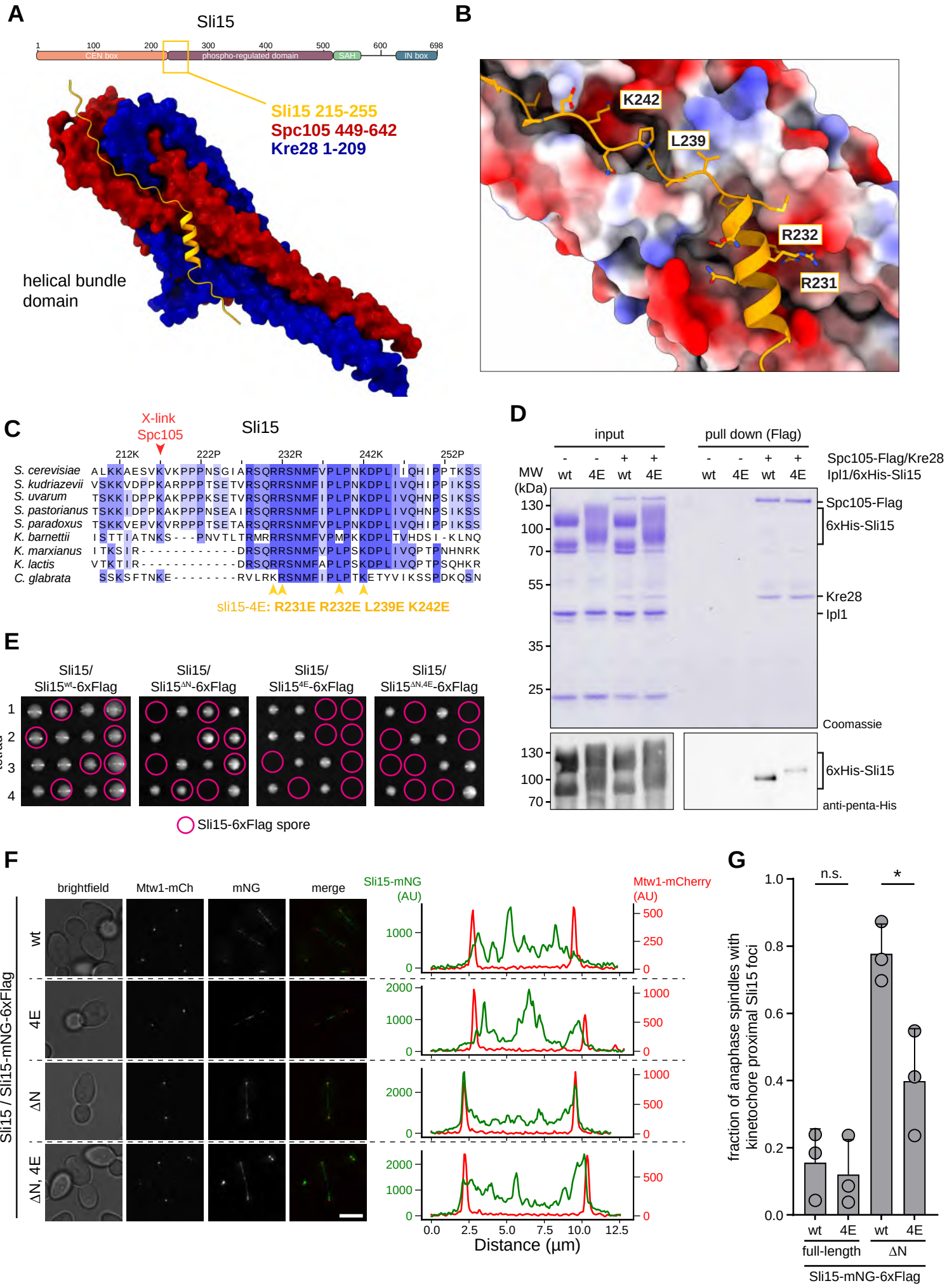
A
Sli15
1
100
200
300
400
500
600
698
CEN box
phospho-regulated domain
SAH
IN box
Sli15 215-255
Spc105 449-642
Kre28 1-209
helical bundle domain
B
K242
L239
R232
R231
C
X-link Spc105
Sli15
212K
222P
232R
242K
252P
S. cerevisiae
S. kudriazevii
S. uvarum
S. pastorianus
S. paradoxus
K. barnettii
K. marxianus
K. lactis
C. glabrata
sli15-4E: R231E R232E L239E K242E
D
input
pull down (Flag)
Spc105-Flag/Kre28
Ipl1/6xHis-Sli15
MW (kDa)
wt
4E
130
100
70
55
35
25
Spc105-Flag
6xHis-Sli15
Kre28
Ipl1
Coomassie
anti-penta-His
E
Sli15/ Sli15wt-6xFlag
Sli15/ Sli15ΔN-6xFlag
Sli15/ Sli15 4E-6xFlag
Sli15/ Sli15ΔN,4E-6xFlag
tetrad
1
2
3
4
Sli15-6xFlag spore
F
brightfield
Mtw1-mCh
mNG
merge
Sli15-mNG (AU)
Mtw1-mCherry (AU)
Sli15 / Sli15-mNG-6xFlag
wt
4E
ΔN
ΔN, 4E
Distance (µm)
G
n.s.
*
fraction of anaphase spindles with kinetochore proximal Sli15 foci
full-length
ΔN
Sli15-mNG-6xFlag

Figure EV4 - refers to Figure 7

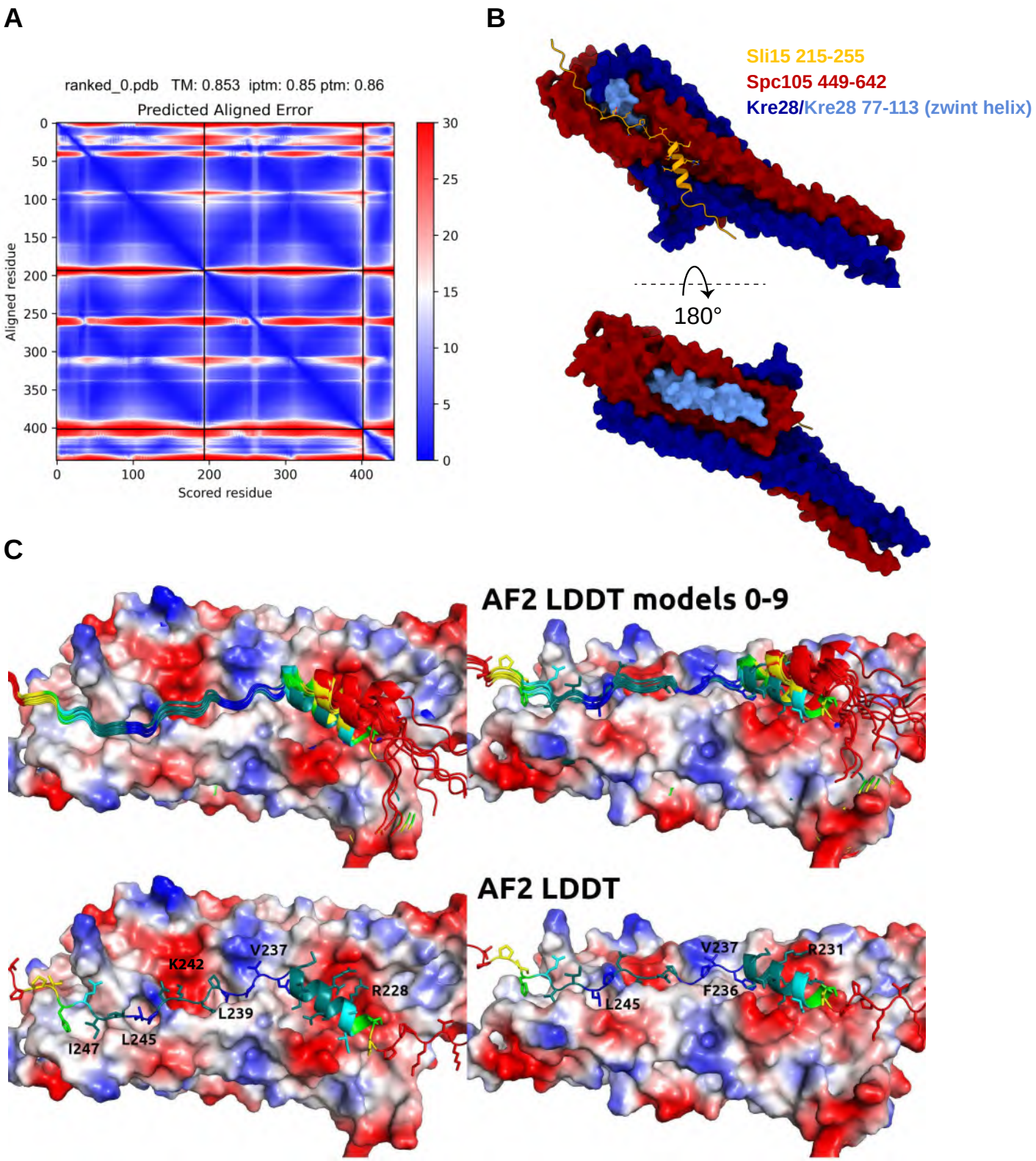

Figure EV5 - refers to Figure 7

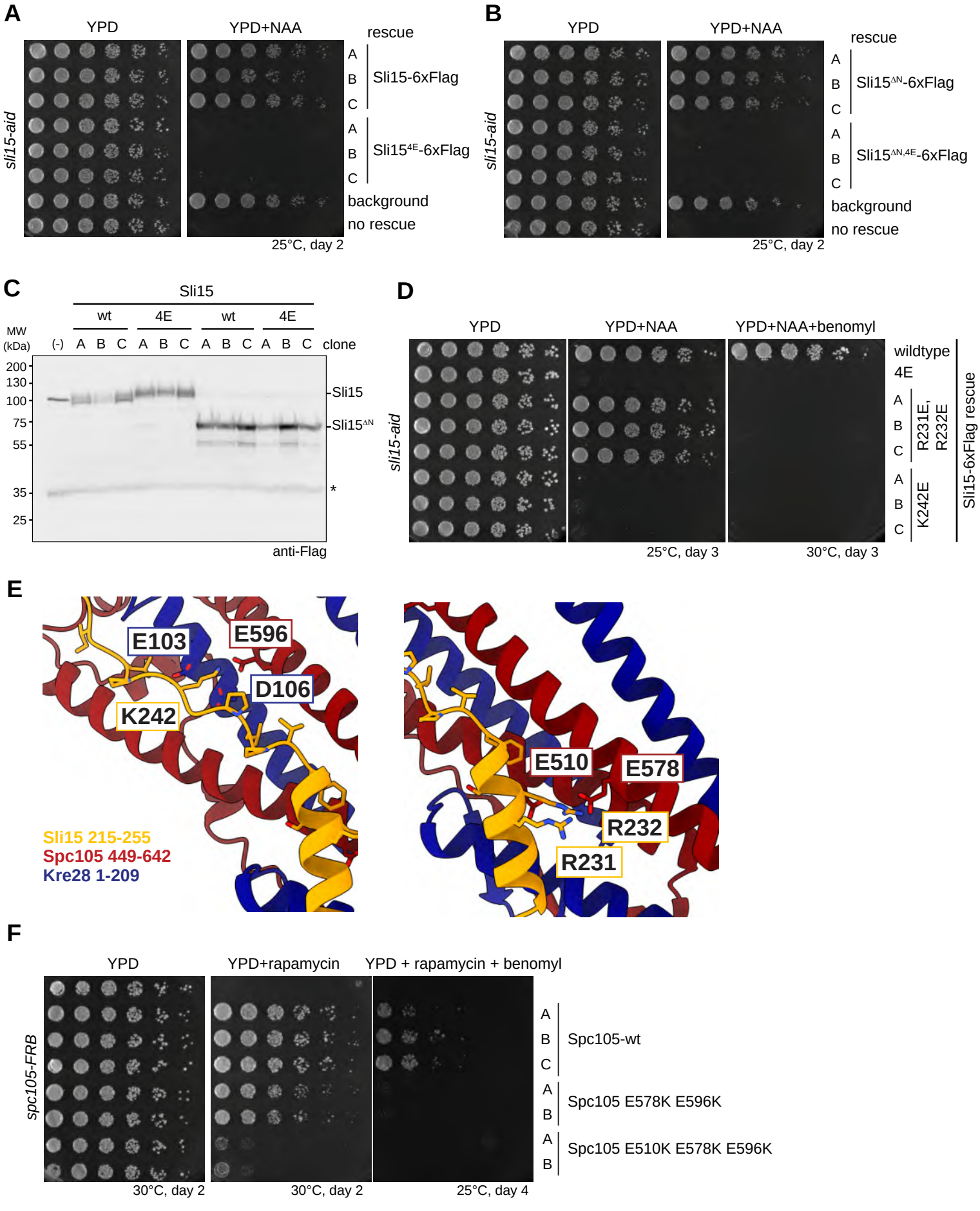

Figure 8

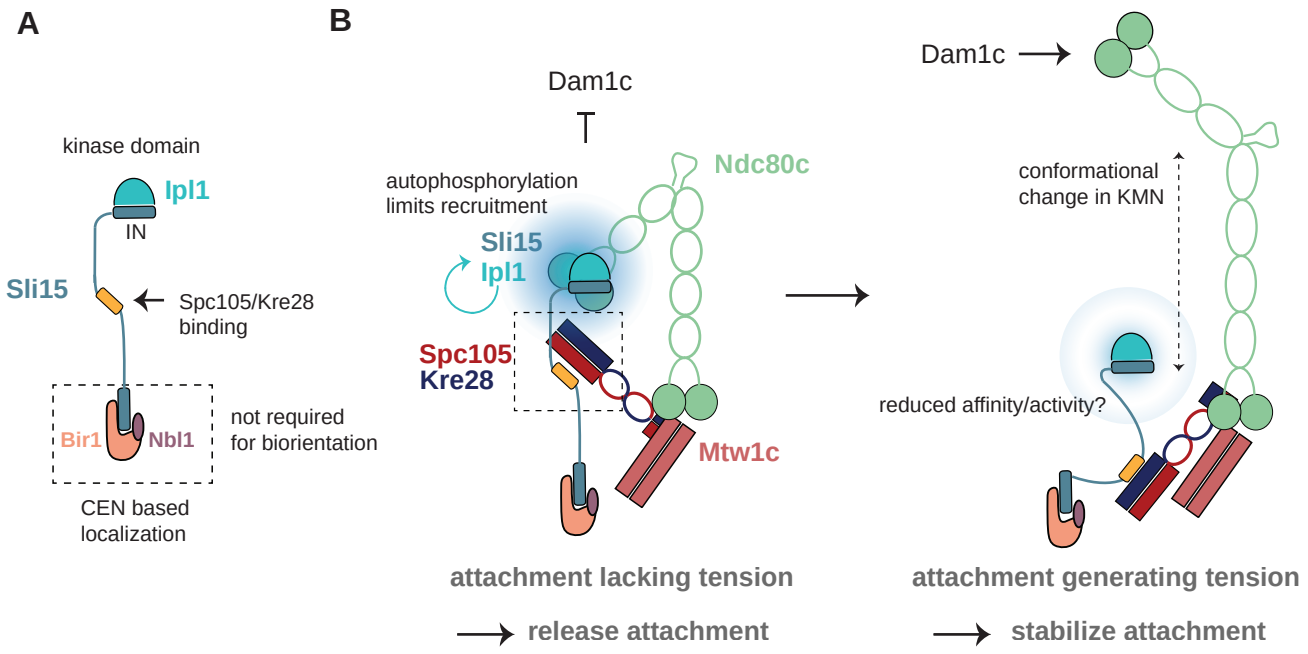
A
kinase domain
Ipl1
IN
Sli15
Spc105/Kre28
binding
Bir1
Nbl1
not required
for biorientation
CEN based
localization
B
Dam1c
Ndc80c
autophosphorylation
limits recruitment
Sli15
Ipl1
Spc105
Kre28
Mtw1c
attachment lacking tension
release attachment
Dam1c
conformational
change in KMN
reduced affinity/activity?
attachment generating tension
stabilize attachment